photostimuli-induced activity gain was quantified as the ratio of the mean $\Delta F/F$ in the last 5 min of the photostimulation period to that in the first 5 min minus 1. We identified neurons that showed significantly higher activity in response to the ChR2 photostimuli than to the light-emitting diode illuminations ($P<0.05$; one-tailed two-sample t-test) and termed them photostimuli-responsive neurons (Fig. 8c). In the potentiation protocol, 56% of imaged neurons were photostimuli-responsive neurons (78 out of 139 neurons in four sessions from four mice), whereas, in the depression protocol, 30% of imaged neurons were photostimuli-responsive neurons (40 out of 132 neurons in four sessions from four mice). Although the photostimuli-responsive neurons in these two protocols had almost identical $\Delta F/F$ at the beginning of the sessions, the photostimuli-induced activity gains of these neurons were significantly positive and negative in the potentiation and depression protocols, respectively (Fig. 8d,e). The activity gain of the other neurons was not significantly different from zero in either protocol (potentiation protocol, $P=0.059$, $n=61$; depression protocol, $P=0.20$, $n=92$; one-sample t-test). The different modulation of photostimuli-responsive neurons in the potentiation and depression protocols was not due to a difference in licking behaviours because the licking frequency around the reward (-1 to -1 s) and after the reward (2 to 4 s) did not change from the first 5 min to the last 5 min in either protocol (Fig. 8f). In addition, 60 photostimuli delivered without any water delivery did not induce substantial changes in the activity gain in the photostimuli-responsive neurons (Fig. 8e); thus, repetitive pairing of neuronal activity with reward delivery at different time intervals was sufficient to recreate RTBM.

Discussion

Here, we demonstrated rapid operant conditioning of single neurons in the rodent motor cortex by two-photon calcium imaging. The physical reward contingency task was introduced in advance, and the mice rapidly learned to increase the activity of target neurons that were not related to the pre-trained movement. The increase in the activity of these neurons was robust; the mean activity increase was $\sim50\%$ of the first 5 min activity. The successful operant conditioning of lever-unrelated neurons is consistent with the fact that cortical neurons with no discernible relation to muscles can be volitionally modulated in the primate motor cortex[9]. In addition, we showed, for the first time, that the timing of neuronal activity relative to the reward is one of the critical factors for the activity change in non-target neurons in microcircuits. The modulation of non-target neurons was bidirectional and was reproduced by repetitive pairing of ChR2 photostimulation with reward.

Recently, operant conditioning of two ensembles in the mouse motor cortex by two-photon calcium imaging was reported, whereby the mouse was conditioned to change the activity of the two ensembles in opposite directions[27]. The temporal dynamics of the activities in the two target ensembles were different to each other, and the conditioning depended on the correlation between them. Therefore, for each non-target neuron, the spatial and temporal associations with the target ensembles were inevitably affected not only by each target ensemble, but also by the relation between the two target ensembles. By contrast, in the present study, the target neuron was a single neuron; therefore the spatial and temporal associations with the target neuron could be unambiguously determined for each non-target neuron. Our results clearly showed that non-target neurons that exhibited high activity synchronous with reward delivery (SR neurons) were reinforced and non-target neurons whose activity followed the reward after 2–4 s (AR neurons) were repressed. The

correlation between SR neurons and the target neuron was higher than that between other non-target neurons and the target neuron; however, the distance to the target neuron was similar across SR, AR and other non-target neurons. This suggests that the microcircuit has the capability to strengthen the activity of neurons that were previously included in the same ensemble without strong spatial constrains, which can explain the variety of behaviours of non-target neurons observed during SNOC in primates[2,3,9,10]. During fast adaptation, which requires changes in behaviours or internal models[28], novel ensembles may be broadly generated based on the structure of pre-existing ensembles. However, our finding that lever-related and lever-unrelated non-target neurons were similarly modulated during the conditioning period suggests that pre-existing ensembles that are not relevant to a novel reward contingency do not necessarily restrict the microcircuit reorganization. We found that a subset of non-target neurons that were not correlated with the target neuron decreased their activity over the conditioning period. The changes in the activity of SR and AR neurons were not due to changes in licking or lever-pull behaviours that might be related to reward prediction. The counterbalance of microcircuit activity may play a role in maintaining a constant overall level of network activity for homeostasis[14,16,29]. Our results suggest that RTBM is possibly one of many processes that underlie rapid reorganization of the L2/3 cortical microcircuit during fast adaptation to environmental changes, which occurs during brain–machine and brain–computer interface learning, motor adaptation and skill learning.

RTBM was recreated by repetitive pairing of the reward with direct stimulation of a random set of neurons in the motor cortex. Although licking behaviours did not change in either protocol, the bidirectional activity changes might be related to reward prediction and reward-absence prediction signals without appearance of any behaviours. However, the proportion of imaged neurons that were photostimuli responsive (56% and 30% in the potentiation and depression protocols, respectively) was larger than the proportion of neurons with high RRAI ($\sim5\%$; Fig. 7d). In addition, reward-modulated neurons were very rarely observed ($\sim3\%$) in the rat forelimb M1 in a self-initiated lever-pull–push task[19]. It is therefore unlikely that the reward-prediction activity had a large effect on the bidirectional changes in the microcircuit. Thus, our results indicate that the motor cortex can be a causal origin of the RTBM without signals from the prefrontal and parietal cortices, which are presumably required for cognitive strategies[5,10]. In the auditory cortex, forward conditioning of pure tone stimulation and electrical stimulation of dopaminergic ventral tegmental neurons increased the size of the cortical area responding to the tone frequency, and backward conditioning reduced the size of the area[30,31]. This bidirectional remodeling may share the same underlying mechanisms as RTBM in the motor cortex, although RTBM in the motor cortex was faster. The dopaminergic projections to the motor cortex are necessary for motor learning[32]. Dopamine uptake in the prefrontal cortex takes up to 5 s[33]; therefore, increased dopamine concentration in the motor cortex may last for the observed time interval between reward delivery and activity in AR neurons. The corticostriatal synapses also show bidirectional plasticity with dopamine release[34], which is necessary for neuroprosthetic skill learning[35]. Dopaminergic projections to the motor cortex and striatum may cooperatively induce bidirectional modulations in L2/3 neurons.

Methods

All mice were provided with food and water *ad libitum* and housed in a 12:12 h light–dark cycle. Mice were not used for other experiments before the study. Mice were anesthetized by intraperitoneal injection of ketamine (74 mg kg^{-1}) and xylazine (10 mg kg^{-1}) before an incision was made in the skin covering the neocortex. After the exposed skull was cleaned, a head plate (Tsukasa Giken, Sizuoka, Japan) was attached to the skull using dental cement (Fujiryu-to BC; GC, Tokyo, Japan, Bistite II; Tokuyama Dental, Tokyo, Japan). The surface of the intact skull was coated with dental adhesive resin cement (Super bond; Sun Medical, Shiga, Japan) to prevent drying. Mice were allowed to recover for 1 day before virus injection. The number of mice per cage was 2–5 before the head plate was attached. After that, mice were single-caged to avoid damage to the head plate and the glass window.

Virus production. GCaMP7 cDNA was cloned from the GCaMP7 vector[20] and inserted into pAAV (Addgene plasmid 26973; a kind gift from Dr K. Deisseroth, Stanford University) to obtain recombinant AAV type 2/1 (rAAV2/1) expressing GCaMP7. The vector plasmid (pAAV-*syn*-GCaMP7) contained GCaMP7 cDNA and the woodchuck hepatitis virus post-transcriptional regulatory element, which was expressed under control of the pan-neuronal human synapsin I promoter (*syn*-GCaMP7). rAAV2/1-*syn*-GCaMP7 (AAV-*syn*-GCaMP7) was produced following triple-transfection of HEK293 cells with pAAV-*syn*-GCaMP7, an adenoviral helper plasmid pAdeno and a chimeric helper plasmid encoding AAV2 rep/AAV1 cap genes (pAAV2-1, gifted to us from Dr J. M. Wilson, University of Pennsylvania)[36], which was mediated by calcium phosphate co-precipitation with active gassing[37]. rAAV2/1-*syn*-GCaMP7 was purified according to previous studies[38,39]. All rAAV2/9 were obtained from the University of Pennsylvania Gene Therapy Program Vector Core.

Virus injection. Thirty minutes before surgery, dexamethasone sodium phosphate (1.32 mg kg^{-1}; to prevent cerebral edema), the antibiotics sulfadiazine (24 mg kg^{-1}) and trimethoprim (4.8 mg kg^{-1}) and the anti-inflammatory carprofen (6 mg kg^{-1}) were administered intraperitoneally. Isoflurane (1%) inhalation was used for anesthesia throughout surgery. A 2-mm diameter circular craniotomy was made over the left rostral motor forelimb area (circle centered $\sim$2.4 mm anterior and $\sim$0.9 mm lateral to bregma) or the left caudal motor forelimb area (circle centered $\sim$0.2 mm anterior and $\sim$1.2 mm lateral to bregma). The dura mater was removed. Before virus injection, a pulled glass pipette (broken and beveled to an outer diameter of $\sim$25–30 µm; Sutter Instruments, California, USA) and a 5 µl Hamilton syringe were back-filled with mineral oil (Nacalai Tesque, Kyoto, Japan) and front-loaded with virus solution. Either 50 nl of AAV-*syn*-GCaMP7 (7.1 $\times$ 10^{12} vector genomes ml^{-1}) or 50 nl of mixed solution containing AAV-*syn*-GCaMP6f (9.0 $\times$ 10^{12} vector genomes ml^{-1}), AAV-flex-ChR2-mCherry (3.8 $\times$ 10^{12} vector genomes ml^{-1}) and AAV-CMV-Cre (2.2 $\times$ 10^{10} vector genomes ml^{-1}) was injected via a syringe pump at a rate of 0.1 µl min^{-1} (KDS310; KD Scientific, Massachusetts, USA) to a depth of 300 µm from the cortical surface. The pipette was inserted vertically and maintained in place for 10 min after the injection. The injection was repeated at 1–3 sites within the rostral motor forelimb area or the caudal motor forelimb area. After the pipette was slowly withdrawn, 4% (w v^{-1}) agarose L (Nippon Gene, Tokyo, Japan) was placed over the craniotomy, a 4.5-mm-diameter glass coverslip (number 0 thickness; Matsunami Glass, Osaka, Japan) was pressed onto the agarose surface[13], and the edges were sealed with dental adhesive resin cement. Mice were then returned to their cages. Mice were allowed to recover and to express sufficient doses of GCaMP7 or GCaMP6f and ChR2 proteins for 2–4 weeks before imaging experiments were performed.

Lever-pull task. Seven AAV-*syn*-GCaMP7-transduced mice were used for the self-initiated lever-pull task, which was modified from a previous study[13]. In brief, water-deprived mice were trained to pull a lever for a distance of 5 mm over a time period of 400 ms to obtain a 4 µl drop of water. The water delivery was accompanied by a small click from the water valve. The animals were required to leave the lever at its original position and wait $>$3 s before pulling the lever again to receive the next water drop.

Optical SNOC. The seven mice injected with AAV-*syn*-GCaMP7 and trained at the lever-pull task were used for SNOC by two-photon calcium imaging (2pSNOC). Two-photon calcium imaging was conducted using a FV1000-MPE system (Olympus, Tokyo, Japan) and a mode-locked Ti:sapphire laser (MaiTai HP; Spectra Physics, California, USA) at a wavelength of 910 nm. A 690-nm shortpass dichroic mirror (Olympus) was used to separate the excitation laser and the emitted fluorescence. Fluorescence emissions were collected using a GaAsP photomultiplier tube (PMT; Hamamatsu Photonics, Shizuoka, Japan). The laser intensity was adjusted to 5–36 mW to maintain a constant baseline level of fluorescence in the neurons. The imaged field was 128–512 $\times$ 128–268 µm (mean, 380 $\times$ 199 µm; $n = 24$ fields from seven mice) and the depth of the imaging plane was 162.5 $\pm$ 45.2 µm below the cortical surface ($n = 24$). The frame duration was 216–311 ms (mean, 292 ms, $n = 24$). The fluorescence intensity of multiple neurons on the monitor of the FV1000-MPE was continuously detected with a machine vision camera (Basler, Ahrensburg, Germany) connected to a personal computer,

and was analyzed in real time using a custom-developed and -deployed program written with the assistance of the LabVIEW vision module (National Instruments, Texas, USA). A region of interest (ROI) containing a single neuron was specified, and the mean fluorescence intensity of this ROI was continually measured. When the fluorescence intensity of the ROI remained under the manually determined threshold (3–6 s.d. of the baseline fluorescence intensity) for $>$1 s and then exceeded the threshold, the mouse was rewarded with two 4-µl drops of water from a spout near the mouth.

Simultaneous two-photon imaging and ChR2 photostimulation. Six mice injected with AAV-*syn*-GCaMP6f, AAV-flex-ChR2-mCherry and AAV-CMV-Cre were used for the simultaneous two-photon calcium imaging and ChR2 photostimulation experiments. Relatively low-titered AAV-CMV-Cre (2.2 $\times$ 10^{10} vector genomes ml^{-1}) was stochastically transduced to a limited number of neurons, and relatively high-titered AAV-flex-ChR2-mCherry (3.8 $\times$ 10^{12} vector genomes ml^{-1}) was used to enable strong expression of ChR2 in a sparse subset of neurons. The water-deprived mice were acclimatized to the head restraint and delivery of water from the spout under a microscope for 2 days before the start of the photostimulation experiments. Two-photon calcium imaging was performed in the same way as in the 2pSNOC experiments, except that multialkali PMTs were used instead of GaAsP PMTs to prevent photodamage. The imaged field was fixed to 320 $\times$ 160 µm ($n = 11$ from six mice) and the depth of the imaged plane was 128.5 $\pm$ 17.5 µm below the cortical surface ($n = 11$). The frame duration was 294 ms. A blue-light source (cat. no. MBL-H-473, OptoEngine LLC, Utah, USA) was used for photostimulation[21,40] and bifurcated 473-nm light-emitting diodes (LEX2-B; BrainVision, Tokyo, Japan) were set in front of both eyes for masking. The frames that included either photostimulation or masking and one subsequent frame were discarded from the analysis. A 480-nm shortpass dichroic mirror (Olympus) was used to separate the excitation blue light and the emitted fluorescence.

Offline processing of imaging data. Analyses were performed using ImageJ software (version 1.45s; National Institutes of Health, Maryland, USA) and MATLAB software (versions R2010a, R2011b, MathWorks, Massachusetts, USA). Image sequences were corrected for focal plane displacements by applying the ImageJ plug-in, TurboReg[41]. ROIs were manually specified. Averaging the fluorescence of all pixels within each ROI resulted in a raw time series, from which time-averaged background fluorescence measured in unstained blood vessels was subtracted. The detrended relative change in fluorescence ($\Delta F/F$) was calculated from the subtracted time series using the eighth percentile value from 15 s before to 15 s after each sample time point[12,13]. Non-negative deconvolution[23] of each $\Delta F/F$ trace was performed using a decay time constant of 1 s and divided by the median absolute deviation of the deconvoluted trace $\times$ 1.3826 $\times$ 2 (2 σ). A value of 1 was subtracted from these values. Then, if the values were negative, they were set to zero. The final values were defined as 'activity'. The ROIs whose activity demonstrated skewness $>$1 were defined as reconstructed neurons[13]. Further analysis was limited to the reconstructed neurons.

In the experiments involving simultaneous two-photon calcium imaging and ChR2 photostimulation, the $\Delta F/F$ trace without deconvolution was used for analysis because the light stimulation interrupted continuous monitoring of fluorescence and, therefore, precluded deconvolution. The $\Delta F/F$ values in interrupted frames were removed from the analysis. For each neuron, the $\Delta F/F$ value 588 ms (two frames) after photostimulation was compared with the $\Delta F/F$ value 588 ms after masking stimulation using a one-tailed two-sample t-test. If $\Delta F/F$ after photostimulation was significantly larger ($P < 0.05$) than $\Delta F/F$ after masking stimulation, the neuron was defined as a photostimuli-responsive neuron. The number of photostimuli-responsive neurons was 14.8 $\pm$ 9.7 ($n = 11$ fields) per field of view (320 $\times$ 160 µm) and this accounted for 43.9% of reconstructed neurons. mCherry fluorescence was detected in 4.9 $\pm$ 2.2 cells ($n = 8$ fields in which mCherry fluorescence was recorded) per field of view (320 $\times$ 160 µm) by *in vivo* two-photon imaging and this accounted for 15.0% of reconstructed neurons; thus, neurons without sufficiently strong mCherry fluorescence should have been included in photostimuli-responsive neurons. ChR2-mCherry-expressing neurons out of the focal plane might also play a role in activating photostimuli-responsive neurons. In 90.2% (156/173) of the photostimuli-responsive neurons, the peak fluorescence value on the first trial was more than half of the peak of the mean fluorescence value on all trials. Thus, the photostimulation immediately evoked activity in the photostimuli-responsive neurons, which eliminates the possibility that the light itself gradually affected the neurons and induced conditioned light responses.

Definition of lever-related and lever-unrelated neurons. Eight hundred and forty reconstructed neurons were categorized according to their association with the lever movement during the pre-conditioning period. The period from 1 s before the onset of the lever-pull movement to 3 s after the lever had returned to the original position was defined as the lever-related period. During the lever-related period, neurons showing activity that was significantly larger ($P < 0.05$ by one-tailed two-sample t-test) than that outside the lever-related period were defined as lever-related neurons. The remaining neurons were defined as lever-unrelated neurons.

Definition of RSI. The 5 s after water delivery was defined as the reward-related period. Spontaneous pairwise correlation was the correlation between the activity of two neurons in reward-unrelated periods of the conditioning period. Activity in reward-related periods was excluded from this analysis to remove any effect of reward-related activity and/or behaviours. The neuronal activity in the first 10 min of the conditioning period was used to calculate RSI(t). Activity in the final 5 min of the conditioning period was excluded to remove any effect of activity gain and reward gain. RSI(t) was defined as the sum of activity in a 0.33 s bin t s after reward delivery divided by the sum of activity in reward-unrelated periods. If the time bin t was included in the reward-related period, RSI(t) was defined as the sum of activity in a 0.33 s bin t s after reward delivery divided by the sum of activity t s after reward delivery and activity in reward-unrelated periods. The duration of the time bin was 0.33 s, which was approximately the duration of a single frame. Because the activity calculated by non-negative deconvolution was ≥ 0, RSI(t) ranged from 0 to 1 by definition.

Analysis of licking behaviour. Licking behaviour was monitored at 30 Hz with an infrared video camera during the 2pSNOC experiments and by electrophysiological methods during the photostimulation experiments. To quantify the number of licks per second from the video data, an ROI that included the tongue was selected within the movie and the number of times that the mean intensity of the ROI exceeded a threshold (the mean of the maximum and minimum values in a data set) was counted. To quantify the number of licks per second from the electrophysiological data, the electropotential difference between the spout and the head of the mouse was measured and sampled by the FV1000-MPE. The number of times that the electropotential exceeded a threshold (the mean of the maximum and minimum values in a data set) was counted.

Statistics. Data are presented as mean ± s.d. Student's t-test, the Wilcoxon signed-rank test, the Wilcoxon rank sum test, Spearman's correlation test, Pearson's correlation test and χ^2-test were used for statistical comparisons. Pairwise comparisons were two-tailed unless otherwise noted. Error bars in graphs represent the s.e.m. ANOVA and post-hoc Tukey's HSD (honestly significant difference) test were used for multiple comparisons. No statistical tests were run to predetermine sample size. Blinding and randomization were not performed.

References

1. Green, A. M. & Kalaska, J. F. Learning to move machines with the mind. *Trends Neurosci.* **34,** 61–75 (2011).
2. Moritz, C. T., Perlmutter, S. I. & Fetz, E. E. Direct control of paralysed muscles by cortical neurons. *Nature* **456,** 639–642 (2008).
3. Fetz, E. E. Operant conditioning of cortical unit activity. *Science* **163,** 955–958 (1969).
4. Fetz, E. E. Volitional control of neural activity: implications for brain–computer interfaces. *J. Physiol.* **579,** 571–579 (2007).
5. Schafer, R. J. & Moore, T. Selective attention from voluntary control of neurons in prefrontal cortex. *Science* **332,** 1568–1571 (2011).
6. Izhikevich, E. M. Solving the distal reward problem through linkage of STDP and dopamine signaling. *Cereb. Cortex* **17,** 2443–2452 (2007).
7. Legenstein, R., Pecevski, D. & Maass, W. A learning theory for reward-modulated spike-timing-dependent plasticity with application to biofeedback. *PLoS Comput. Biol.* **4,** e1000180 (2008).
8. Legenstein, R., Chase, S. M., Schwartz, A. B. & Maass, W. A reward-modulated hebbian learning rule can explain experimentally observed network reorganization in a brain control task. *J. Neurosci.* **30,** 8400–8410 (2010).
9. Fetz, E. E. & Baker, M. A. Operantly conditioned patterns on precentral unit activity and correlated responses in adjacent cells and contralateral muscles. *J. Nuerophysiol* **36,** 179–204 (1973).
10. Hwang, E. J., Bailey, P. M. & Andersen, R. A. Volitional control of neural activity relies on the natural motor repertoire. *Curr. Biol.* **23,** 353–361 (2013).
11. Arduin, P.-J., Frégnac, Y., Shulz, D. E. & Ego-Stengel, V. 'Master' neurons induced by operant conditioning in rat motor cortex during a brain-machine interface task. *J. Neurosci.* **33,** 8308–8320 (2013).
12. Dombeck, D. A., Graziano, M. S. & Tank, D. W. Functional clustering of neurons in motor cortex determined by cellular resolution imaging in awake behaving mice. *J. Neurosci.* **29,** 13751–13760 (2009).
13. Hira, R. et al. Spatiotemporal dynamics of functional clusters of neurons in the mouse motor cortex during a voluntary movement. *J. Neurosci.* **33,** 1377–1390 (2013).
14. Lütcke, H., Margolis, D. J. & Helmchen, F. Steady or changing? Long-term monitoring of neuronal population activity. *Trends Neurosci.* **36,** 375–384 (2013).
15. Komiyama, T. et al. Learning-related fine-scale specificity imaged in motor cortex circuits of behaving mice. *Nature* **464,** 1182–1186 (2010).
16. Masamizu, Y. et al. Two distinct layer-specific dynamics of cortical ensembles during learning of a motor task. *Nat. Neurosci.* **17,** 987–994 (2014).
17. Gage, G. J., Ludwig, K. A., Otto, K. J., Ionides, E. L. & Kipke, D. R. Naive coadaptive cortical control. *J. Neural Eng.* **2,** 52–63 (2005).
18. Gradinaru, V. et al. Targeting and readout strategies for fast optical neural control in vitro and in vivo. *J. Neurosci.* **27,** 14231–14238 (2007).
19. Isomura, Y. et al. Reward-modulated motor information in identified striatum neurons. *J. Neurosci.* **33,** 10209–10220 (2013).
20. Ohkura, M. et al. Genetically encoded green fluorescent Ca^{2+} indicators with improved detectability for neuronal Ca^{2+} signals. *PLoS One* **7,** e51286 (2012).
21. Hira, R. et al. In vivo optogenetic tracing of functional corticocortical connections between motor forelimb areas. *Front. Neural Circuits* **7,** 55 (2013).
22. Tennant, K. A. et al. The organization of the forelimb representation of the C57BL/6 mouse motor cortex as defined by intracortical microstimulation and cytoarchitecture. *Cereb. Cortex* **21,** 865–876 (2011).
23. Vogelstein, J. T. et al. Fast nonnegative deconvolution for spike train inference from population calcium imaging. *J. Neurophysiol.* **104,** 3691–3704 (2010).
24. O'Connor, D. H., Peron, S. P., Huber, D. & Svoboda, K. Neural activity in barrel cortex underlying vibrissa-based object localization in mice. *Neuron* **67,** 1048–1061 (2010).
25. Schultz, W. Multiple dopamine functions at different time courses. *Annu. Rev. Neurosci.* **30,** 259–288 (2007).
26. Chen, T.-W. et al. Ultrasensitive fluorescent proteins for imaging neuronal activity. *Nature* **499,** 295–300 (2013).
27. Clancy, K. B., Koralek, A. C., Costa, R. M., Feldman, D. E. & Carmena, J. M. Volitional modulation of optically recorded calcium signals during neuroprosthetic learning. *Nat. Neurosci.* **17,** 807–809 (2014).
28. Gandolfo, F., Li, C.-S., Benda, B., Schioppa, C. P. & Bizzi, E. Cortical correlates of learning in monkeys adapting to a new dynamical environment. *Proc. Natl Acad. Sci. USA* **97,** 2259–2263 (2000).
29. Abbott, L. F. & Nelson, S. B. Synaptic plasticity: taming the beast. *Nat. Neurosci.* **3,** 1178–1183 (2000).
30. Bao, S., Chan, V. T. & Merzenich, M. M. Cortical remodelling induced by activity of ventral tegmental dopamine neurons. *Nature* **412,** 79–83 (2001).
31. Bao, S., Chan, V. T., Zhang, L. I. & Merzenich, M. M. Suppression of cortical representation through backward conditioning. *Proc. Natl. Acad. Sci. USA* **100,** 1405–1408 (2003).
32. Molina-Luna, K. et al. Dopamine in motor cortex is necessary for skill learning and synaptic plasticity. *PLoS One* **4,** e7082 (2009).
33. Garris, P. & Wightman, R. Different kinetics govern dopaminergic transmission in the amygdala, prefrontal cortex, and striatum: an in vivo voltammetric study. *J. Neurosci.* **14,** 442–450 (1994).
34. Shen, W., Flajolet, M., Greengard, P. & Surmeier, D. J. Dichotomous dopaminergic control of striatal synaptic plasticity. *Science* **321,** 848–851 (2008).
35. Koralek, A. C., Jin, X., Long, II J. D., Costa, R. M. & Carmena, J. M. Corticostriatal plasticity is necessary for learning intentional neuroprosthetic skills. *Nature* **483,** 331–335 (2012).
36. Xiao, W. et al. Gene therapy vectors based on adeno-associated virus type 1. *J. Virol.* **73,** 3994–4003 (1999).
37. Okada, T. et al. Large-scale production of recombinant viruses by use of a large culture vessel with active gassing. *Hum. Gene Ther.* **16,** 1212–1218 (2005).
38. Okada, T. et al. Scalable purification of adeno-associated virus serotype 1 (AAV1) and AAV8 vectors, using dual ion-exchange adsorptive membranes. *Hum. Gene Ther.* **20,** 1013–1021 (2009).
39. Masamizu, Y. et al. Local and retrograde gene transfer into primate neuronal pathways via adeno-associated virus serotype 8 and 9. *Neurosci* **193,** 249–258 (2011).
40. Hira, R. et al. Transcranial optogenetic stimulation for functional mapping of the motor cortex. *J. Neurosci. Methods* **179,** 258–263 (2009).
41. Thevenaz, P., Ruttimann, U. E. & Unser, M. A pyramid approach to subpixel registration based on intensity. *IEEE Trans. Image Process* **7,** 27–41 (1998).

Author contributions

R.H. and M.M. designed the experiments. R.H. and F.O. conducted the experiments. M.O. and J.N. generated GCaMP7. Y.M. and T.O. generated AAV1-GCaMP7. R.H. analyzed the data. R.H. and M.M. wrote the paper, along with comments from all authors.

Additional information

The following resources related to this article are available online at www.sciencemag.org (this information is current as of September 18, 2014):

Updated information and services, including high-resolution figures, can be found in the online version of this article at:
http://www.sciencemag.org/content/345/6203/1505.full.html

Supporting Online Material can be found at:
http://www.sciencemag.org/content/suppl/2014/09/17/345.6203.1505.DC1.html

This article **cites 43 articles**, 19 of which can be accessed free:
http://www.sciencemag.org/content/345/6203/1505.full.html#ref-list-1

This article appears in the following **subject collections:**
Medicine, Diseases
http://www.sciencemag.org/cgi/collection/medicine

29. A. Timmer, R. J. Hilsden, J. Cole, D. Hailey, L. R. Sutherland, *BMC Med. Res. Methodol.* **2**, 7 (2002).
30. K. P. Lee, E. A. Boyd, J. M. Holroyd-Leduc, P. Bacchetti, L. A. Bero, *Med. J. Aust.* **184**, 621–626 (2006).
31. K. Okike, M. S. Kocher, C. T. Mehlman, J. D. Heckman, M. Bhandari, *J. Bone Joint Surg.* **90**, 595–601 (2008).
32. K. Dickersin, S. Chan, T. C. Chalmers, H. S. Sacks, H. Smith Jr., *Control. Clin. Trials* **8**, 343–353 (1987).
33. K. Dickersin, Y. I. Min, C. L. Meinert, *JAMA* **267**, 374–378 (1992).
34. K. Dickersin, Y. I. Min, *Online J. Curr. Clin. Trials* **1993**, 50 (1993).
35. R. M. D. Smyth *et al.*, *BMJ* **342** (jan06 1), c7153 (2011).
36. H. Cooper, K. DeNeve, K. Charlton, *Psychol. Methods* **2**, 447–452 (1997).
37. G. V. B. Glass, B. McGaw, M. L. Smith, *Meta Analysis in Social Research* (Sage, Beverly Hills, CA, 1981).
38. The rate at which research-initiated proposals are approved by the peer reviewers engaged by TESS is provided in the supplementary materials.
39. TESS archive; www.tessexperiments.org.
40. Materials and methods are available as supplementary materials on *Science* Online.
41. K. Casey, R. Glennerster, E. Miguel, *Q. J. Econ.* **127**, 1755–1812 (2012).

NEUROMUSCULAR DISEASE

DOK7 gene therapy benefits mouse models of diseases characterized by defects in the neuromuscular junction

Sumimasa Arimura,[1] Takashi Okada,[2] Tohru Tezuka,[1] Tomoko Chiyo,[2] Yuko Kasahara,[2] Toshiro Yoshimura,[3] Masakatsu Motomura,[4] Nobuaki Yoshida,[5] David Beeson,[6] Shin'ichi Takeda,[2] Yuji Yamanashi[1]*

The neuromuscular junction (NMJ) is the synapse between a motor neuron and skeletal muscle. Defects in NMJ transmission cause muscle weakness, termed myasthenia. The muscle protein Dok-7 is essential for activation of the receptor kinase MuSK, which governs NMJ formation, and *DOK7* mutations underlie familial limb-girdle myasthenia (*DOK7* myasthenia), a neuromuscular disease characterized by small NMJs. Here, we show in a mouse model of *DOK7* myasthenia that therapeutic administration of an adeno-associated virus (AAV) vector encoding the human *DOK7* gene resulted in an enlargement of NMJs and substantial increases in muscle strength and life span. When applied to model mice of another neuromuscular disorder, autosomal dominant Emery-Dreifuss muscular dystrophy, *DOK7* gene therapy likewise resulted in enlargement of NMJs as well as positive effects on motor activity and life span. These results suggest that therapies aimed at enlarging the NMJ may be useful for a range of neuromuscular disorders.

The neurotransmitter acetylcholine (ACh) is released from the presynaptic motor nerve terminal and binds to ACh receptors (AChRs) on the postsynaptic muscle membrane of the neuromuscular junction (NMJ), which forms in the central region of each myotube (1, 2). To achieve efficient neuromuscular transmission, AChRs must be densely clustered on the postsynaptic membrane (1, 2). Impaired AChR clustering is associated with disorders of neuromuscular transmission, including subtypes of congenital myasthenic syndromes and myasthenia gravis (2–4). The muscle-specific receptor tyrosine kinase MuSK is required for the formation and maintenance of NMJs (1, 2).

The cytoplasmic protein Dok-7 (downstream of tyrosine kinases 7) is an essential activator of the receptor kinase MuSK, and mice lacking Dok-7 form no NMJs (5–8). Recessive loss- or reduction-of-function mutations in the human *DOK7* gene underlie a limb-girdle type of congenital myasthenic syndrome, *DOK7* myasthenia, a disorder characterized by NMJs that are about half the normal size (7, 9, 10). In contrast to many NMJ channelopathies (11), *DOK7* myasthenia is not associated with abnormalities in the function and local density of AChRs or the quantal release per unit size of the endplates (the region of synaptic specialization on the myotube). These observations suggest that *DOK7* myasthenia should be classified as a synaptopathy rather than a channelopathy (2, 7). Interestingly, there is ac-

cumulating evidence that NMJ structural defects may be a common feature of other neuromuscular disorders (12–18), including muscular dystrophy (MD), amyotrophic lateral sclerosis (ALS), spinal muscular atrophy (SMA), and age-related muscle weakness or sarcopenia. Indeed, studies of patients with autosomal dominant Emery-Dreifuss muscular dystrophy (AD-EDMD) and a mouse model of this disease have produced data suggestive of inefficient neuromuscular transmission (12). Because the size of NMJs is an important determinant of NMJ function (2), these observations raise the possibility that enlargement of the synaptic area may mitigate muscle weakness associated with defective NMJ structure.

We previously generated Dok-7 transgenic (Tg) mice that overexpress Dok-7 uniformly throughout the skeletal muscle under the control of the human skeletal α-actin (HSA) promoter (6). Using these mice, we found that forced expression of Dok-7 in vivo enhanced the activation of muscle-specific kinase MuSK and subsequent NMJ formation at the correct, central region of muscle fibers in embryos (6). Consistent with this, Dok-7 Tg mice showed greatly enlarged NMJs at 12 weeks of age (fig. S1A). Because exogenous Dok-7 was expressed only in the skeletal muscle (6), these data indicate that forced expression of Dok-7 in muscle triggers not only intramuscular signaling but also retrograde signaling that enlarges motor axon terminals. Interestingly, although these mice have enlarged NMJs, they did not exhibit obvious defects in motor activity, as determined by wire-hang and rotarod tests (fig. S1, B and C). Together, these findings suggest that Dok-7–mediated enhancement of NMJ formation merits investigation as a possible therapeutic approach for neuromuscular disorders associated with an NMJ synaptopathy.

To facilitate Dok-7–mediated NMJ formation in the muscle, we generated AAV-D7, a recombinant adeno-associated virus (AAV) serotype 9 (AAV9) vector carrying the human *DOK7* gene tagged with enhanced green fluorescent protein (EGFP) under the control of the cytomegalovirus (CMV) promoter. This promoter shows higher activity in skeletal muscle than the HSA promoter (19). The AAV vector is a powerful tool for delivering therapeutic genes to skeletal muscle and other tissues (20, 21). We first treated C2C12 myotubes

[1]Division of Genetics, The Institute of Medical Science, The University of Tokyo, Tokyo, Japan. [2]Department of Molecular Therapy, National Institute of Neuroscience, National Center of Neurology and Psychiatry, Tokyo, Japan. [3]Department of Occupational Therapy, Nagasaki University School of Health Sciences, Nagasaki, Japan. [4]Department of Electrical and Electronics Engineering, Faculty of Engineering, Nagasaki Institute of Applied Science, Nagasaki, Japan. [5]Laboratory of Developmental Genetics, The Institute of Medical Science, The University of Tokyo, Tokyo, Japan. [6]Neurosciences Group, Weatherall Institute of Molecular Medicine, University of Oxford, Oxford, UK.
*Corresponding author. E-mail: yyamanas@ims.u-tokyo.ac.jp

with AAV-D7 and observed an increase in the number of AChR clusters (fig. S2), as expected from previous work (5, 7, 9). We next treated 8-week-old wild-type (WT) mice with 4.0 × 10¹¹ viral genomes (vg) of AAV-D7, delivered by a single intravenous injection, and compared them with control, untreated mice. One week after the injection, NMJs were clearly enlarged in the central region of the diaphragm muscle of AAV-D7–treated mice, with exogenous expression of Dok-7 throughout the myotubes (fig. S3 and Fig. 1, A and B). MuSK activation was augmented in the muscle as judged by elevated phosphorylation of MuSK and AChR, the latter known to be dependent on MuSK activation (Fig. 1, C and D). These results demonstrate that forced expression of Dok-7 in adult mice promotes MuSK-mediated formation of NMJs, leading to their enlargement within a week of AAV-D7 treatment. WT mice treated with AAV-D7 did not show any abnormalities in motor activity, as determined by grip strength, wire-hang, and rotarod tests (fig. S4), or in histology of the skeletal muscle, heart, and liver, which are the major target tissues of this AAV9 vector in mice (fig. S5) (22). We confirmed exogenous expression of Dok-7 in the heart (fig. S6) and in skeletal muscle (fig. S3 and Fig. 1A) after AAV-D7 treatment.

To investigate whether forced expression of Dok-7 and subsequent enlargement of NMJs in vivo mitigates disease progression after onset of DOK7 myasthenia, we generated Dok-7 knock-in (KI) mice homozygous for the frameshift mutation (c.1124_1127dupTGCC), which corresponds to the most prevalent mutation in patients (fig. S7) (7, 10, 23–25). Dok-7⁺/ᴷᴵ and littermate WT mice displayed no obvious abnormal phenotype. By contrast, Dok-7ᴷᴵ/ᴷᴵ mice (Dok-7 KI mice) exhibited characteristic features of severe muscle weakness: These mice died between postnatal day 13 (P13) and P20, exhibited about 25% of the body weight of WT mice at P12, and developed apparent disturbance in gait by P9 (fig. S8). Unlike Dok-7⁺/ᴷᴵ and littermate WT mice, Dok-7 KI mice were too weak for the measurement of muscle strength. Furthermore, they showed abnormally small NMJs lacking postsynaptic folding (figs. S9 and S10), a pathological feature seen in patients with DOK7 myasthenia (26). The c.1124_1127dupTGCC mutation is a reduction-of-function mutation in terms of MuSK activation in C2C12 myotubes (7, 9). Consistent with this, Dok-7 KI mice exhibited decreased MuSK activity in skeletal muscle, as judged by attenuated phosphorylation of AChR and MuSK (fig. S11) (see below). Thus, the Dok-7 KI mice develop defects similar to those found in patients with DOK7 myasthenia, although the mice (hereafter referred to as "DOK7 myasthenia mice") exhibit a more severe phenotype.

To determine whether DOK7 gene therapy provides beneficial effects to DOK7 myasthenia mice, we administered 2.0 × 10¹¹ vg of AAV-D7 by intraperitoneal injection to the animals at P9 to P12. At P9, these mice required at least 10 s to right themselves after being placed on their side, confirming disease onset. A single-dose treatment with AAV-D7 led to marked recovery of the DOK7
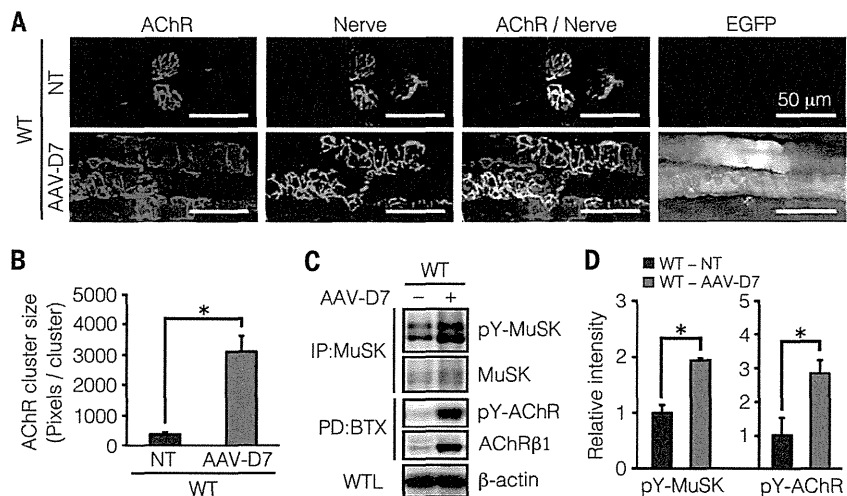
Fig. 1. AAV-D7 treatment promotes MuSK-mediated NMJ formation. WT mice were treated or untreated with 4.0 × 10¹¹ vg of AAV-D7 at P56 and subjected to the following assays at P63. (**A**) Whole-mount staining of NMJs on the diaphragm muscle. Axons and nerve terminals (green) were stained with antibodies to neurofilament and synaptophysin, and AChRs (red) were labeled with α-bungarotoxin (BTX). Expression of Dok-7 tagged with EGFP (gray) was monitored by EGFP. NT, not treated. (**B**) Quantified data for the size of each AChR cluster in the diaphragm muscle (n = 30 microscopic fields in 6 mice; male = 3, female = 3). (**C**) Immunoblotting for tyrosine phosphorylation of MuSK or AChR and for β-actin in the hind-limb muscle. MuSK immunoprecipitates (IP) from whole-tissue lysates (WTL) of the hind-limb muscle were subjected to immunoblotting for phosphotyrosine (pY) and MuSK. AChRs pulled down with BTX-Sepharose (PD) from WTL were subjected to immunoblotting for pY or the β1 subunit of AChR. (**D**) Quantified data for tyrosine phosphorylation of MuSK and AChR in the hind-limb muscle (n = 3 mice; male = 1 to 2, female = 1 to 2). Values in (B) and (D) are means ± SD. *P < 0.05 by Student's t test.
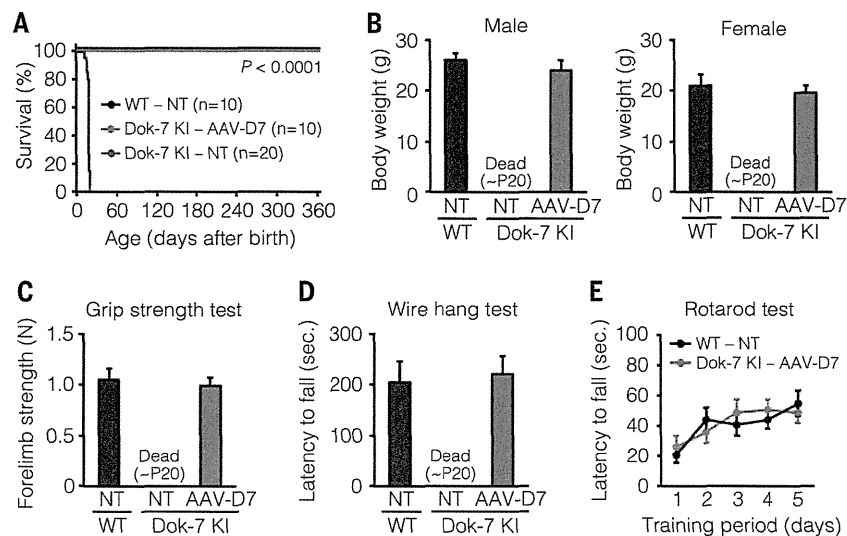
Fig. 2. Dok-7 therapy restores motor activity and survival of DOK7 myasthenia mice. Mice were treated or untreated with 2.0 × 10¹¹ vg of AAV-D7 at P9 to P12. (**A**) Kaplan-Meier survival curves of WT littermates and Dok-7 KI mice (DOK7 myasthenia mice) (n = 10 to 20 mice; male = 4 to 10, female = 6 to 10). NT, not treated. (**B**) Body weight at P56 (n = 4 to 6 mice; male = 5, female = 4 to 6). (**C** to **E**) Motor activity at P56 determined by (C) grip strength, (D) wire-hang, and (E) rotarod tests (n = 10 mice; male = 4 to 5, female = 5 to 6). P value (A) was calculated by log-rank test (Dok-7 KI − NT versus Dok-7 KI − AAV-D7). Values in (B) to (E) are means ± SD.

— 83 —

myasthenia mice. All AAV-D7–treated mice survived for at least 1 year with no apparent abnormality, whereas all untreated and AAV-EGFP–treated

control mice died by P20 (Fig. 2A and fig. S12). Indeed, body weight and motor activity—as determined by grip strength, wire-hang, and rotarod

tests—of AAV-D7–treated mice approximated those of age-matched WT controls by P56 (Fig. 2, B to E). Similarly, forced expression of a *DOK7* transgene

Fig. 3. Dok-7 therapy promotes MuSK-mediated NMJ formation in *DOK7* myasthenia mice. Mice were treated or untreated with 2.0×10^{11} vg of AAV-D7 at P9 and subjected to the following assays at P14. (**A**) Immunoblotting for tyrosine phosphorylation of MuSK or AChR and for β-actin in the hind-limb muscle. Experiments were performed as in Fig. 1C. (**B**) Quantified data for tyrosine phosphorylation of MuSK and AChR in the hind-limb muscle ($n = 3$ mice; male = 1 to 2, female = 1 to 2). (**C**) Whole-mount staining of NMJs on the diaphragm muscle. Axons and nerve terminals (green), AChRs (red), and Dok-7 tagged with EGFP (gray) were visualized as in Fig. 1A. (**D**) Quantified data for the size of each AChR cluster in the diaphragm muscle ($n = 30$ microscopic fields in 6 mice; male = 3, female = 3). Values in (B) and (D) are means ± SD. *$P < 0.05$ by analysis of variance (ANOVA) and Dunnett's test.
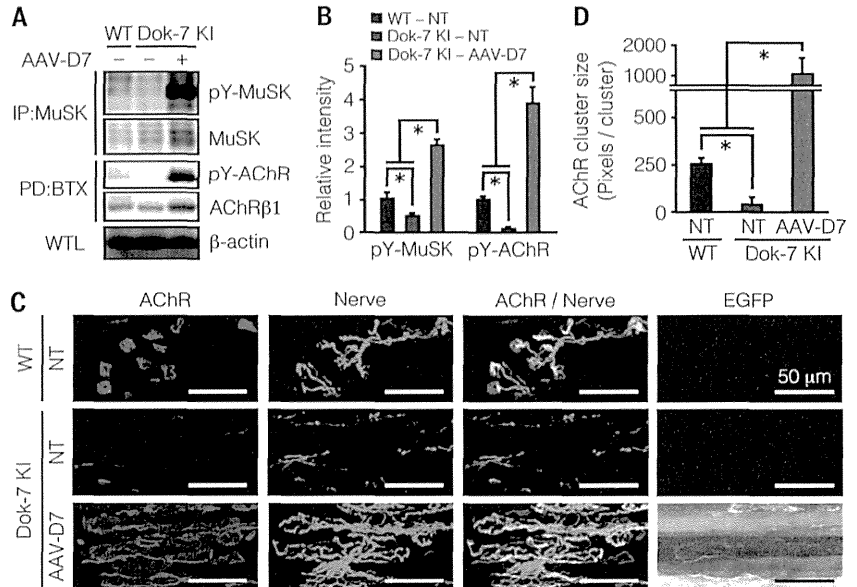
Fig. 4. The effect of Dok-7 therapy in a mouse model of AD-EDMD. Mice were treated or untreated with 4.0×10^{11} vg of AAV-D7 at P16 and subjected to the following assays. (**A**) Kaplan-Meier survival curves of WT littermates and Lmna KO mice (AD-EDMD mice) ($n = 19$ to 20 mice; male = 9 to 12, female = 8 to 11). NT, not treated. (**B** and **C**) Motor activity at P35, determined by (B) wire-hang and (C) rotarod tests ($n = 8$ to 10 mice; male = 4 to 6, female = 4 to 5). (**D**) Whole-mount staining of NMJs on the diaphragm muscle at P42. Axons and nerve terminals (green), AChRs (red), and Dok-7 tagged with EGFP (gray) were visualized as in Fig. 1A. (**E**) Quantified data for the size of each AChR cluster in the diaphragm muscle at P42 ($n = 30$ microscopic fields in 6 mice; male = 3 to 4, female = 2 to 3). (**F**) Immunoblotting for tyrosine phosphorylation of MuSK or AChR and for β-actin in the hind-limb muscle at P42. Experiments were performed as in Fig. 1C. (**G**) Quantified data for tyrosine phosphorylation of MuSK and AChR in the hind-limb muscle at P42 ($n = 3$ mice; male = 1 to 2, female = 1 to 2). *P* value (A) was calculated by log-rank test (Lmna KO – NT versus Lmna KO – AAV-D7). Values in (B), (C), (E), and (G) are means ± SD. *$P < 0.05$ by analysis of variance (ANOVA) and Dunnett's test.

— 84 —
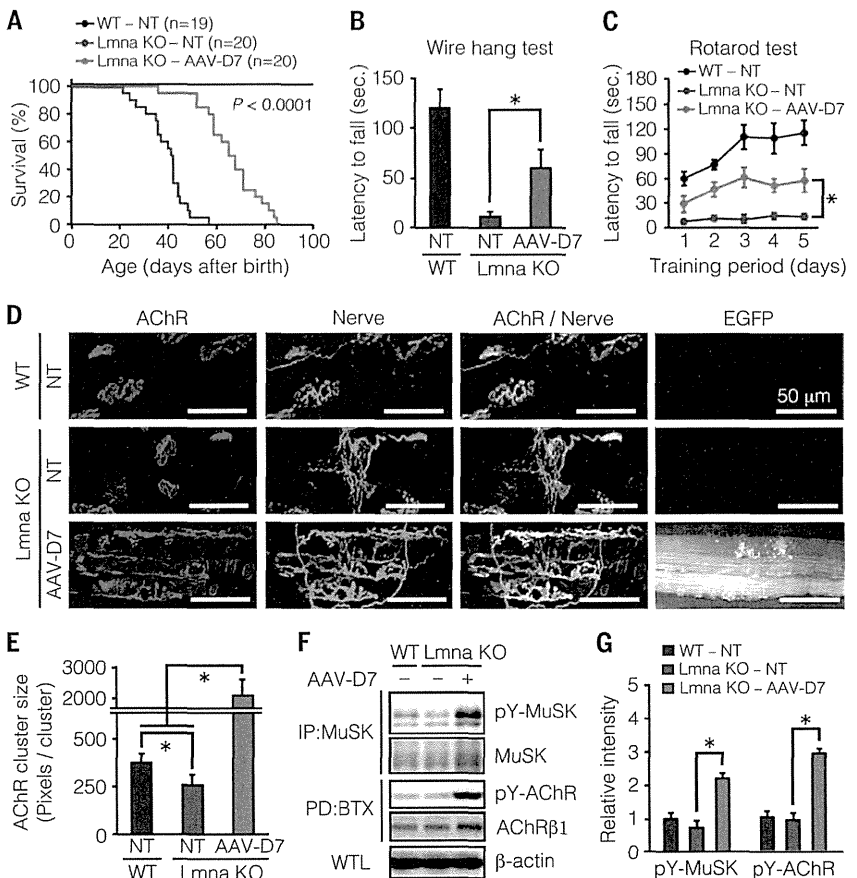
specifically in skeletal muscle restored survival and motor activity of *DOK7* myasthenia mice as determined by wire-hang and rotarod tests, indicating that muscle-specific expression of Dok-7 is sufficient to rescue these mice (fig. S13, A to C).

We next investigated whether AAV-D7 treatment promotes activation of MuSK and subsequent enlargement of NMJs in *DOK7* myasthenia mice. We found that MuSK and AChR phosphorylation was strongly elevated in *DOK7* myasthenia mice just 5 days after treatment with AAV-D7 (Fig. 3, A and B). Consistent with this, NMJs were greatly enlarged in *DOK7* myasthenia mice within 5 days of treatment (Fig. 3, C and D, and fig. S14) and remained enlarged at 8 weeks of age (fig. S15). Together, these data demonstrate that treatment with AAV-D7 (hereafter referred to as "Dok-7 therapy") facilitates MuSK-mediated NMJ formation, resulting in stable enlargement of NMJs, restoration of motor activity, and enhanced survival of *DOK7* myasthenia mice.

Because AAV-D7 enlarges NMJs not only in *DOK7* myasthenia mice but also in WT mice, we hypothesized that Dok-7 therapy might be applicable to other types of neuromuscular disorders that are associated with abnormalities of NMJ structure but not caused by *DOK7* mutations. As noted above, AD-EDMD is one such candidate. AD-EDMD is caused by mutations in the *LMNA* gene, which encodes lamin A/C, an important determinant of interphase nuclear architecture (*27*). Patients with AD-EDMD develop cardiac defects and skeletal muscle weakness (*28*). Although pacemaker and implantable cardioverter defibrillator (ICD) insertion helps address the cardiac defects (*29*), there is no effective treatment for skeletal muscle weakness. Histology and gene expression profiles of muscle biopsies from patients with AD-EDMD are suggestive of alterations in NMJ structure (*12, 30, 31*).

We studied a mouse model of AD-EDMD (hereafter referred to as "AD-EDMD mice") that is genetically deficient in lamin A/C and that has structurally abnormal and functionally inefficient NMJs (*12, 30*). At P16, we administered 4.0×10^{11} vg of AAV-D7 into the AD-EDMD mice by a single intraperitoneal injection. Disease onset was confirmed in each AD-EDMD mouse at P16, when the animals showed hind-limb paralysis and required at least 10 s to right themselves after being placed on their sides. We found that Dok-7 therapy prolonged survival of AD-EDMD mice (Fig. 4A). Mice receiving Dok-7 therapy, but not those receiving AAV-EGFP treatment, lived an average of 29 days longer than untreated mice ($P < 0.0001$, log-rank test) (Fig. 4A and fig. S16). In addition, Dok-7 therapy increased latency to fall of AD-EDMD mice, as determined by wire-hang and rotarod tests by 49 s and 44 s, respectively, over untreated mice ($P < 0.05$, Dunnett's test) (Fig. 4, B and C), indicating enhanced motor activity. Forced expression of Dok-7 specifically in skeletal muscle via a transgene also enhanced AD-EDMD mouse survival and motor activity, as determined by wire-hang and rotarod tests, indicating that muscle-specific expression of Dok-7 is sufficient to benefit these mice (fig. S13, D to F).

Dok-7 therapy enhanced MuSK activation and enlarged NMJs in the skeletal muscle within 26 days of treatment (Fig. 4, D to G), and the NMJs in control, untreated AD-EDMD mice were significantly smaller than those in WT mice (Fig. 4, D and E). Electrocardiographic and histological analyses showed that Dok-7 therapy did not benefit heart function in AD-EDMD mice (fig. S17). It is possible that the beneficial effects of Dok-7 therapy on muscle weakness are partially masked in these mice by heart failure, which, as noted above, would be treatable in patients with AD-EDMD by pacemaker and ICD insertion (*29*). These findings suggest that Dok-7 therapy might be beneficial for patients with AD-EDMD.

The mechanisms through which Dok-7 therapy alleviates muscle weakness in mouse models of *DOK7* myasthenia and AD-EDMD remain to be determined. We speculate that, in addition to an effect on the postsynaptic region of muscle, the mechanism likely involves retrograde signaling from the muscle to the nerve. This idea is consistent with the observation that enlargement of the nerve terminals at NMJs is seen in the Dok-7 Tg mice that overexpress Dok-7 only in the skeletal muscle, as well as in AAV-D7–treated mice.

Recent studies of mouse models of ALS and SMA revealed that peripheral motor nerve degeneration first manifests as reduction of the nerve terminal area with subsequent denervation at NMJs, and then proceeds proximally, a pattern known as "dying-back" pathology (*32, 33*). Consistent with this, autopsies of patients with ALS or SMA suggest that motor neuron pathology begins at the distal axon and proceeds proximally (*32, 34*). Because AAV-D7 has the potential to enlarge the nerve terminals at NMJs, it is tempting to speculate that Dok-7 therapy may counteract the "dying-back" pathology at NMJs and be beneficial in these multifactorial disorders of mostly unknown etiology. Interestingly, in a recent study of the SOD1 (superoxide dismutase 1) G93A Tg mouse model of ALS, it was reported that a modest, muscle-specific increase in MuSK expression via a transgene delayed denervation at NMJs and improved motor activity, but not survival, of the mice (*35*). However, a previous study had shown that higher-level expression of MuSK in the muscle induces scattered NMJ formation throughout myotubes, leading to severe muscle weakness and ultimately to death (*36*). Dok-7 gene therapy may be a safer approach because it greatly facilitates correct, centrally localized NMJ enlargement without lethal effects for more than 1 year in *DOK7* myasthenia mice (Figs. 2A and 3C and figs. S14 and S15).

AAV-mediated gene transfer to skeletal muscle can result in long-term expression of the therapeutic gene. For instance, in a patient with hemophilia B, AAV-mediated expression of factor IX was detected even 10 years after a single intramuscular injection (*37*). In addition, although AAV capsid, rather than transgene, is the antigen that is targeted by the host immune responses in humans, this process can be controlled by a short course of treatment with immunosuppressant without loss of transgene expression (*38*), raising

prospects for long-term use of these vectors in therapies.

Our findings demonstrate that elevated Dok-7 expression, or any equivalent method that stably and safely enlarges the NMJ, has potential as a therapy for a variety of neuromuscular disorders that feature defects in NMJ structure, including those of unknown etiology. Such NMJ-targeted therapies could be administered alone or in combination with other therapies.

REFERENCES AND NOTES

1. S. J. Burden, *Genes Dev.* **12**, 133–148 (1998).
2. C. R. Slater, *Handb. Clin. Neurol.* **91**, 27–101 (2008).
3. A. G. Engel, K. Ohno, S. M. Sine, *Nat. Rev. Neurosci.* **4**, 339–352 (2003).
4. P. Cavalcante, P. Bernasconi, R. Mantegazza, *Curr. Opin. Neurol.* **25**, 621–629 (2012).
5. K. Okada et al., *Science* **312**, 1802–1805 (2006).
6. A. Inoue et al., *Sci. Signal.* **2**, ra7 (2009).
7. D. Beeson et al., *Science* **313**, 1975–1978 (2006).
8. Y. Yamanashi, T. Tezuka, K. Yokoyama, *J. Biochem.* **151**, 353–359 (2012).
9. J. Hamuro et al., *J. Biol. Chem.* **283**, 5518–5524 (2008).
10. D. Selcen et al., *Ann. Neurol.* **64**, 71–87 (2008).
11. G. G. Celesia, *Clin. Neurophysiol.* **112**, 2–18 (2001).
12. A. Méjat et al., *J. Cell Biol.* **184**, 31–44 (2009).
13. P. C. Ghedini et al., *Muscle Nerve* **38**, 1585–1594 (2008).
14. J. D. Gumerson et al., *Hum. Mol. Genet.* **22**, 757–768 (2013).
15. F. Saito et al., *J. Neurochem.* **101**, 1712–1722 (2007).
16. L. R. Fischer et al., *Exp. Neurol.* **185**, 232–240 (2004).
17. S. Kariya et al., *Hum. Mol. Genet.* **17**, 2552–2569 (2008).
18. Y. C. Jang, H. Van Remmen, *Exp. Gerontol.* **46**, 193–198 (2011).
19. J. N. Hagstrom et al., *Blood* **95**, 2536–2542 (2000).
20. M. Nonnenmacher, T. Weber, *Gene Ther.* **19**, 649–658 (2012).
21. F. Mingozzi, K. A. High, *Nat. Rev. Genet.* **12**, 341–355 (2011).
22. C. Zincarelli, S. Soltys, G. Rengo, J. E. Rabinowitz, *Mol. Ther.* **16**, 1073–1080 (2008).
23. J. S. Müller et al., *Brain* **130**, 1497–1506 (2007).
24. J. Palace et al., *Brain* **130**, 1507–1515 (2007).
25. M. Srour et al., *Neuromuscul. Disord.* **20**, 453–457 (2010).
26. C. R. Slater et al., *Brain* **129**, 2061–2076 (2006).
27. B. Burke, C. L. Stewart, *Annu. Rev. Genomics Hum. Genet.* **7**, 369–405 (2006).
28. H. J. Worman, G. Bonne, *Exp. Cell Res.* **313**, 2121–2133 (2007).
29. C. Meune et al., *N. Engl. J. Med.* **354**, 209–210 (2006).
30. T. Sullivan et al., *J. Cell Biol.* **147**, 913–920 (1999).
31. F. J. Ramos et al., *Sci. Transl. Med.* **4**, 144ra103 (2012).
32. L. M. Murray, K. Talbot, T. H. Gillingwater, *Neuropathol. Appl. Neurobiol.* **36**, 133–156 (2010).
33. C. Cifuentes-Diaz et al., *Hum. Mol. Genet.* **11**, 1439–1447 (2002).
34. G. Bruneteau et al., *Brain* **136**, 2359–2368 (2013).
35. M. J. Pérez-García, S. J. Burden, *Cell Reports* **2**, 497–502 (2012).
36. N. Kim, S. J. Burden, *Nat. Neurosci.* **11**, 19–27 (2008).
37. G. Buchlis et al., *Blood* **119**, 3038–3041 (2012).
38. A. C. Nathwani et al., *N. Engl. J. Med.* **365**, 2357–2365 (2011).

nature
neuroscience

Two distinct layer-specific dynamics of cortical ensembles during learning of a motor task

Yoshito Masamizu[1,2,9], Yasuhiro R Tanaka[1,2,9], Yasuyo H Tanaka[1,2], Riichiro Hira[1,2], Fuki Ohkubo[1-3], Kazuo Kitamura[2,4,5], Yoshikazu Isomura[2,6], Takashi Okada[7,8] & Masanori Matsuzaki[1-3]

The primary motor cortex (M1) possesses two intermediate layers upstream of the motor-output layer: layer 2/3 (L2/3) and layer 5a (L5a). Although repetitive training often improves motor performance and movement coding by M1 neuronal ensembles, it is unclear how neuronal activities in L2/3 and L5a are reorganized during motor task learning. We conducted two-photon calcium imaging in mouse M1 during 14 training sessions of a self-initiated lever-pull task. In L2/3, the accuracy of neuronal ensemble prediction of lever trajectory remained unchanged globally, with a subset of individual neurons retaining high prediction accuracy throughout the training period. However, in L5a, the ensemble prediction accuracy steadily improved, and one-third of neurons, including subcortical projection neurons, evolved to contribute substantially to ensemble prediction in the late stage of learning. The L2/3 network may represent coordination of signals from other areas throughout learning, whereas L5a may participate in the evolving network representing well-learned movements.

M1 is the most prominent motor-output area of the cerebral cortex. In M1, L2/3 and L5a constitute intermediate layers upstream of layer 5b (L5b), the major motor-output layer. L2/3 and L5a transmit excitatory flow to L5b, but much less information is transmitted in the reverse direction, that is, from L5b to L2/3 or L5a[1,2]. Although L2/3 and L5a are reciprocally connected in M1, only L5a projects to subcortical regions such as the striatum[2]. During motor learning, the microcircuits of M1 are thought to self-organize to integrate various types of signals related to motor planning, motor primitives and sensory feedback into motor output[3-6]. In fact, when repetitive training is used to improve motor performance, M1 is functionally and structurally reorganized[7-11]. However, it is challenging to identify L5a neurons and record their activity *in vivo*, and it remains unknown how the neuronal activities of L2/3 and L5a of M1 are reorganized during learning of a motor task.

The ability to predict movement by monitoring motor cortical ensemble activity often improves with motor learning[12-15]. Furthermore, representation of movement in single L2/3 neurons in M1 changes dynamically during motor learning (over six sessions of a sensorimotor discrimination task)[16]. The single-neuron representation of movement in L5 of M1 is unreliable during the first 3 d of a two-choice movement task, but the accuracy of prediction improves during this period[14]. Functional and structural reorganization in L5 of M1 is prominent in the late stages of motor learning, after performance has plateaued[10,11]. We hypothesize that this change in the predictive accuracy of neuronal ensembles is achieved by one of two models in which the predictive accuracies

of single-neuron activities variously change[12-17]. The first model is the rank-stable evolving model, which is based on the concept that single-neuron representations of movement are relatively stable[18,19]. In this model, a subset of neurons greatly contributes to the ensemble representation in both the early and late stages of learning. Neurons representing motor primitives or sensory feedback that are necessarily linked to movement continuously contribute to the ensemble representation, and their predictive accuracy rank[20] remains high throughout learning. The second model is the rank-changing evolving model, in which a subset of neurons rises through the predictive accuracy rankings[19]. In the late stage of learning, these neurons contribute to the ensemble representation more substantially than the neurons that were highly ranked in the early stages of learning.

Mouse forelimb M1, also known as the caudal forelimb area[21,22], is a subdivision of M1 in which low-intensity intracortical microstimulation elicits forelimb movements rather than other body movements[21,22]. Its activity is necessary for the performance of a forelimb movement (lever pull) task and many neurons in the rodent forelimb M1 exhibit forelimb movement-associated activity[21,23]. We conducted two-photon calcium imaging in L2/3 and L5a of the forelimb M1 while mice practiced a self-initiated lever-pull task (requiring forelimb use) for 14 consecutive days. L2/3 and L5a were identified according to the cortical depth of the imaging plane. We found that ensemble and single-neuron activities that predicted the lever trajectory were dynamically reorganized in two distinct layer-specific manners during long-term training.

— 86 —

ARTICLES

RESULTS

Mice were trained over 14 sessions (1 h d^{-1}) to use their right fore-limb to pull a lever over a distance of 5 mm for 700 ms to acquire a water reward (**Supplementary Movies 1** and **2**). Training was initiated 2–3 weeks after injection of an adeno-associated virus (AAV) 2/1 encoding GCaMP3 (ref. 24) into the left forelimb M1. As the training progressed, the success rate and number of successful trials increased and the median time interval between successful trials decreased (**Fig. 1a–c**). These task performance parameters began to plateau by session 10, and substantial differences were observed between the early (sessions 1–4) and late (sessions 11–14) sessions (**Fig. 1d–f**).

Two-photon calcium imaging was performed on the left forelimb M1 of nine mice for 14 training sessions without any apparent distortion of the vasculature structure (**Fig. 2a**). Data were obtained from seven L2/3 fields and seven L5a fields (**Fig. 2b** and **Supplementary Table 1**). We imaged L5a, which was defined as the upper region of L5 containing large neurons (**Fig. 2c**), at a depth of 503 ± 29 μm from the cortical surface. Sessions with greatly displaced focal planes were removed and the remaining (more than seven) sessions were analyzed for each field (L2/3, 11.3 ± 2.0 sessions, n = 7 fields from 6 mice; L5a, 11.7 ± 2.3 sessions, n = 7 fields from 6 mice). After motion correction[21,25,26], a region of interest (ROI) for each active neuron was semi-automatically determined on the basis of cell shape and the correlation between the intensities of nearby pixels (**Fig. 2d,e** and **Supplementary Fig. 1**). The number of reconstructed neurons was similar in early and late sessions (L2/3, 40.3 ± 24.4 versus 44.4 ± 16.1, P = 1.0, n = 7 fields from 6 mice; L5a, 53.2 ± 17.4 versus 50.8 ± 25.3, P = 1.0, n = 7 fields from 6 mice, sign test). Fluorescence intensity and fluorescence variability of the reconstructed neurons were also similar in early and late sessions (ROI intensity: L2/3, 727 ± 143 versus 725 ± 144, P = 1.0, n = 7 fields from 6 mice; L5a, 681 ± 138 versus 679 ± 122, P = 0.81, n = 7 fields from 6 mice; mean coefficient of variation of baseline intensity of individual ROIs: L2/3, 0.039 ± 0.012 versus 0.040 ± 0.015, P = 0.94, n = 7 fields from 6 mice; L5a, 0.037 ± 0.015 versus 0.035 ± 0.0098, P = 0.58, n = 7 fields from 6 mice; Wilcoxon signed-rank test). These results indicate that two-photon imaging was stable over the repeated training sessions. Calcium transients in single neurons that were associated with the lever pull were detected in both L2/3 and L5a in early and late sessions (**Fig. 2f,g** and **Supplementary Fig. 2**). *In vivo* cell-attached recordings and *in vitro* whole-cell recordings confirmed that calcium transients were correlated with neuronal firing (**Supplementary Fig. 3a–d**), as shown in previous reports[16,26]. The mean half-decay time of calcium transients (inferred by decon-

volution[27]) was similar in early and late sessions (L2/3, 372 ± 45 ms versus 373 ± 50 ms, P = 0.70, n = 7 fields from 6 mice; L5a, 375 ± 45 ms versus 379 ± 57 ms, P = 0.67, n = 7 fields from 6 mice; Student's t test). In addition, the relative change in fluorescence ($\Delta F/F$) and its signal-to-noise ratio in individual neurons during non–lever-pull periods (from 1 s after the end of a lever pull to 1 s before the onset of the next lever pull) showed only a slight change from the early to late sessions in both layers (**Supplementary Fig. 3e,f**). These results indicate that the neuronal responsiveness did not deteriorate over repeated sessions in either layer (see Online Methods).

We next assessed the effect of repetitive training on the neuronal coding of movement. Forelimb (forepaw) movements that were not directly involved in the lever-pull movement were infrequent throughout the training sessions (**Supplementary Fig. 4a**). In the strength of the correlation between lever movements and forelimb movements (evaluated from infrared video camera recordings), there was no difference throughout training (**Supplementary Fig. 4b,c**). In addition, forelimb movements related to lever pulling were reliable and stable throughout training (**Supplementary Fig. 4d**). These results indicate that the lever movement provided a good representation of the forelimb movement. Thus, we next determined whether the accuracy of the lever trajectory predicted from neuronal ensemble activity improved with learning. In each session and in each imaged field, we predicted lever trajectory with a nonlinear support vector regression (SVR) model[28] that uses inferred spike events obtained from deconvolution of $\Delta F/F$ of multiple neurons (**Fig. 3a,b** and **Supplementary Modeling**). To evaluate the predictive information carried by the neurons (I_{ensemble}), we calculated the mutual information between predicted and recorded lever trajectories[29,30] (**Supplementary Modeling** and **Supplementary Fig. 5**). I_{ensemble} increased as a function of the number of neurons in the ensemble (**Fig. 3c**), which is similar to the hand-trajectory predictions made from cortical ensemble activity in the primate[13,31]. In L2/3, there was no substantial change in I_{ensemble} from the early to late sessions (**Fig. 3d**). In contrast, in L5a, I_{ensemble} was substantially higher in the late sessions than in the early sessions (**Fig. 3d**). We also confirmed this result using alternative analytical methods, including a squared correlation coefficient instead of mutual information (**Fig. 3e**) and multilinear regression instead of SVR (**Fig. 3f**). These methods are often used for motor decoding[13,31] and support the validity of our results.

In the predictive information carried by L5a neurons for reward timing (that is, the mutual information between predicted and actual reward timings), there was not a substantial difference between early and late sessions (**Fig. 3g**). In a similar self-initiated

Figure 1 Learning of a lever-pull task. (a–c) The mean success rate (a), the number of successful trials (b) and the median time interval between successful trials (c; n = 9 mice for all). Error bars indicate s.e.m. (d–f) The success rate (d), the number of successful trials (e) and the median time interval between successful trials (f) in sessions 1–4 (early) and sessions 11–14 (late), after normalization to the value in the early sessions. Each gray line indicates an individual mouse. Thick black lines indicate the mean across mice. Significant differences were observed between the early and late sessions (success rate, P = 0.012; successful trials, P = 0.004; interval time, P = 0.004; n = 9 mice, Wilcoxon signed-rank test). *P < 0.05.

— 87 —
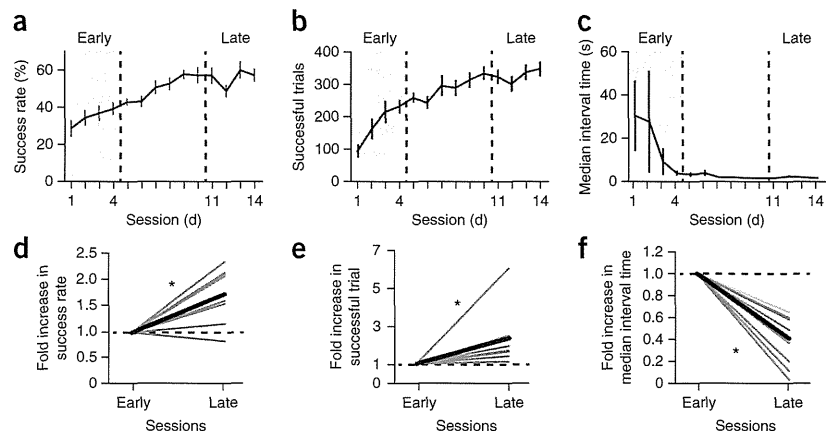
Figure 2 Long-term *in vivo* two-photon imaging of forelimb M1 neurons. (a) Representative vasculature images obtained on day 14 after craniotomy (the first training day) and day 90 after craniotomy. In this mouse, training finished on day 27 after craniotomy. Scale bar represents 500 µm. (b) All imaged fields overlaid on a schematic dorsal view of the left hemisphere of the cortex. L2/3 imaged fields are blue and purple and L5a imaged fields are red and purple. Each of the three purple fields (1, 2 and 3) represents L2/3 and L5a fields in the same horizontal location from the same animal. (c) A representative profile of the size of the neuronal soma as a function of the depth from the cortical surface. 100 GCaMP3-expressing neurons were randomly chosen from a set of *XYZ* two-photon images of forelimb M1 *in vivo*. The axial step size for *XYZ* images was 4 µm. The area of the soma in the *XY* plane at the center of the soma was measured for each neuron. The curve denotes the fitted sigmoidal function. (d) Top, representative two-photon images of an L2/3 field from training session 2 and training session 14. The field was 162 µm from the cortical surface. Scale bar represents 50 µm. Bottom, contours of all ROIs for the reconstructed neurons within this field. Ten neurons that were monitored in more than seven training sessions, including the two displayed sessions, are numbered. (e) Top, representative two-photon images of an L5a field from training session 2 and training session 11. The field was 500 µm from the cortical surface. Scale bar represents 50 µm. (f,g) Representative traces of motion-corrected calcium transients in ten L2/3 neurons in sessions 2 and 14 (f) and ten L5a neurons in sessions 2 and 11 (g). These neurons correspond to the neurons numbered in d and e. Calcium transients of additional neurons are shown in **Supplementary Figure 2**. The lever trajectory, reward timing and occurrence of licking behaviors are shown in the bottom three traces. Period with similar lever trajectories in the two sessions for each field are presented.
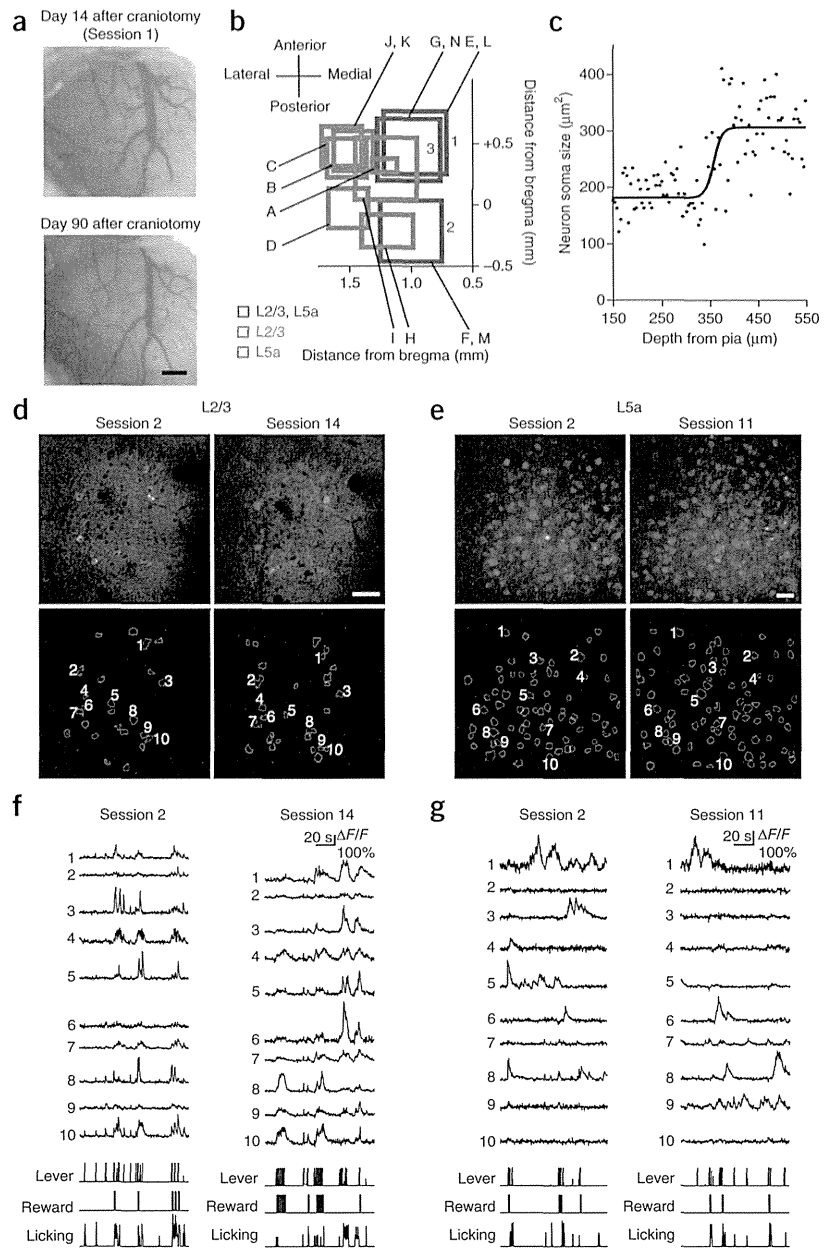

lever-pull-push task performed by rats, reward-modulated neurons were very rarely observed (~3%) in the forelimb M1 (ref. 32). Thus, it is unlikely that reward-modulated L5a neurons have a large effect on the increase in L5a $I_{ensemble}$ of lever movement.

To determine whether the changes in $I_{ensemble}$ are associated with progress in motor task learning, we calculated the fold increase in $I_{ensemble}$ in each session relative to $I_{ensemble}$ averaged over the early sessions for each field. The fold increase in $I_{ensemble}$ was plotted against the fold increase in each task performance parameter in each session relative to the one averaged over the early sessions (**Fig. 4**). The fold increase in L5a $I_{ensemble}$ was correlated with the fold increase in success rate, the number of successful trials and the median interval time, whereas the fold increase in L2/3 $I_{ensemble}$ was not correlated with the fold increase of any task performance parameter. The difference between layers and the variability across different imaged fields in each layer was not a result of differences in the horizontal location of the imaged fields or the experimental conditions (**Supplementary Fig. 6** and **Supplementary Table 1**). Thus, no consistent changes in

L2/3 $I_{ensemble}$ were observed as learning progressed, whereas increases in L5a $I_{ensemble}$ were associated with improved task performance.

The correlation between the timing of lever movements and licking behavior was substantially higher in the late sessions than in the early sessions (**Supplementary Fig. 7a–g**). This indicates that licking behaviors became more strongly associated with lever movements as learning progressed. In fact, mutual information between the recorded lick rate and the lick rate predicted from neuronal activity increased from the early to late sessions in L5a, but not in L2/3 (**Supplementary Fig. 7h**). However, licking was preceded by lever-pull movement in both the early and late sessions (**Supplementary Fig. 7f,i**). In the forelimb M1, licking-related neurons are much less common than lever movement–related neurons[21]. Thus, although neurons associated with licking behaviors, but not with lever-pull movement, may have contributed to the

— 88 —

Figure 3 Changes in $I_{ensemble}$ during learning. (a) Analytical procedures to calculate the prediction accuracy of ensemble activity for the lever movement. In each imaging session, $\Delta F/F$ of individual neurons in a given imaging field (left top) during the lever-pull task were deconvoluted to calculated inferred spike events (left bottom). For each neuron, values were linearly normalized to set the minimum at 0 and the maximum at 1. The lever trajectory was predicted using SVR with the inferred spike events of multiple neurons (right bottom). The prediction accuracy was quantified as the mutual information ($I_{ensemble}$) between the recorded lever trajectory (right top) and the predicted lever trajectory (right bottom). (b) Representative traces of the recorded lever trajectory (gray) and the lever trajectory predicted from 20 neurons (black) in L2/3 (left) and L5a (right) in training session 3 (top row) and training session 11 (bottom row). (c) $I_{ensemble}$ as a function of the number of neurons in the ensemble in a representative L2/3 field and a representative L5a field. The fields are the same as those shown in **b**. Each line represents a training session ($n = 14$ sessions for L2/3 and $n = 12$ sessions for L5a). Colors denote the learning stage: green, early (sessions 1–4); yellow, middle (sessions 5–10); orange, late (sessions 11–14). (d) $I_{ensemble}$ averaged over early and late sessions for each field (L2/3, $P = 1.0$, $n = 7$ fields from 6 mice; L5a, $P = 0.016$, $n = 7$ fields from 6 mice, sign test). Thick lines indicate the fields shown in **b** and **c**. The numbers indicate the fields that were obtained from the same horizontal locations for L2/3 and L5a (purple fields in **Fig. 2b**). $*P < 0.05$. (e) Squared correlation coefficient (R^2) between the recorded lever trajectory and the lever trajectory predicted by the SVR averaged over early and late sessions for each imaged field (L2/3, $P = 0.13$, $n = 7$ fields from 6 mice; L5a, $P = 0.016$, $n = 7$ fields from 6 mice, sign test). $*P < 0.05$. (f) The mutual information ($I_{ensemble}$) between the recorded lever trajectory and the lever trajectory predicted by multilinear regression averaged over early and late sessions for each imaged field (L2/3, $P = 0.45$, $n = 7$ fields from 6 mice; L5a, $P = 0.016$, $n = 7$ fields from 6 mice, sign test). $*P < 0.05$. (g) The mutual information ($I_{ensemble}$) between the actual reward timing and the reward timing predicted from neuronal activity averaged over early and late sessions for each imaged field (L2/3, $P = 0.13$, $n = 7$ fields from 6 mice; L5a, $P = 0.45$, $n = 7$ fields from 6 mice, sign test).
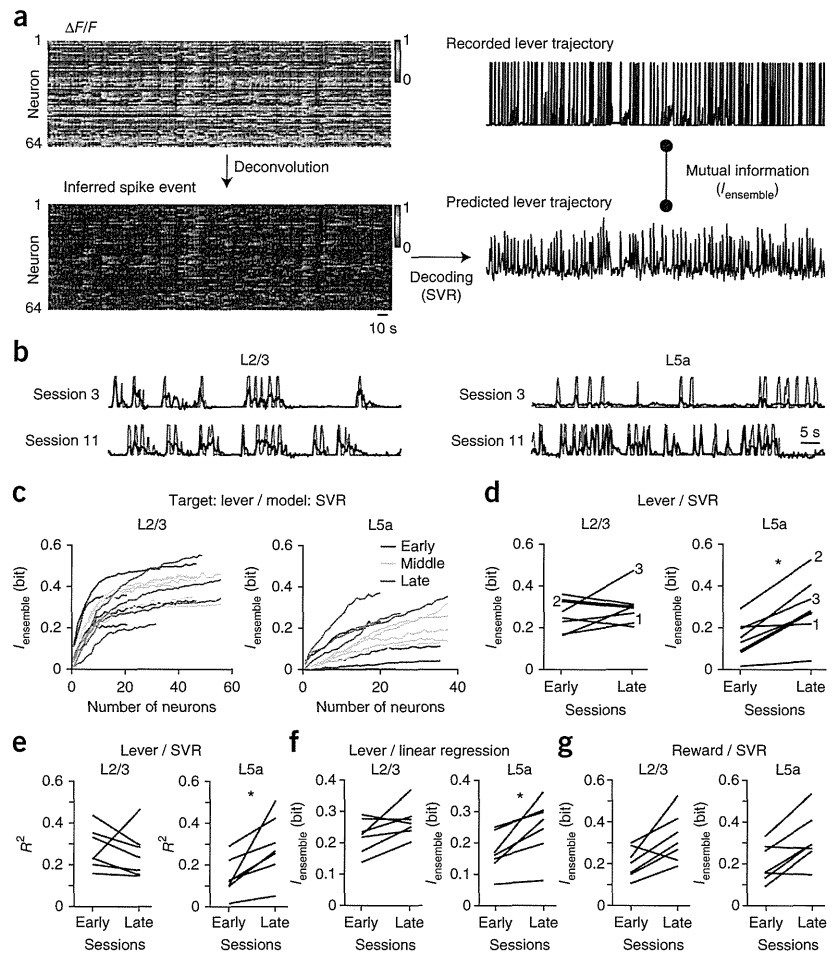
$I_{ensemble}$ of lever movement, we believe that the change in $I_{ensemble}$ of lever movement observed over the early to late sessions primarily represents the reorganization of neuronal activity in the forelimb M1 that occurred as a result of motor task learning.

Next, to determine how each neuron changes its predictive information (I_{single}) during learning, we analyzed I_{single} of neurons that were monitored in more than seven training sessions, including at least one early session and one late session (pursued neurons; $n = 126$ pursued neurons in L2/3 and $n = 187$ pursued neurons in L5a). Neurons that increased or decreased I_{single} across sessions (Spearman's rank correlation coefficient ≥ 0.4 or ≤ -0.4) were defined as increase or decrease neurons, respectively (**Fig. 5a** and **Supplementary Table 2**). The proportion of increase and decrease neurons was substantially different between layers (**Fig. 5b**). In L2/3, there was a similar proportion of increase and decrease neurons (19% versus 17%, $P = 0.77$; estimated from the distribution obtained from 3,000 bootstrap samples in which 126 neurons were sampled with replacement from 126 neurons containing 24 increase and 22 decrease neurons; **Fig. 5b**), suggesting that the overall change in L2/3 I_{single} was balanced across all imaged fields. In contrast, in L5a, there was a higher proportion of increase neurons

than decrease neurons (33% versus 3%, $P < 0.001$; estimated from the distribution from 3,000 bootstrap samples in which 187 neurons were sampled with replacement from 187 neurons containing 63 increase and 5 decrease neurons; **Fig. 5b**). Associations between the classification of pursued neurons and their baseline activities were not detected (**Supplementary Fig. 8**). Rather, the mean activity of L5a increase neurons during successful lever-pull movements was significantly higher in the late sessions than in the early sessions (Z scored activity, 0.12 ± 0.42 in the early sessions versus 0.42 ± 0.67 in the late sessions, $P < 0.001$, $n = 63$ neurons, Wilcoxon signed-rank test; **Fig. 5c,d**). Thus, many L5a increase neurons displayed an increase in activity associated with lever-pull movements during learning.

To verify the contribution of L5a increase neurons to the increase in $I_{ensemble}$ during training sessions, we calculated $I_{ensemble}$ from ten randomly chosen L5a neurons, including increase neurons, in each session in each field (total 70 sessions in six fields of L5a from five mice that contained more than nine pursued neurons). We then recalculated $I_{ensemble}$ from the same ten L5a neurons, but replaced increase neurons with other randomly chosen L5a neurons. This replacement significantly decreased the correlation between the fold increase in

Figure 4 Relation between the fold increase in $I_{ensemble}$ and the fold increase in task performance. (a–c) The fold increase in success rate (a), number of successful trials (b) and median time interval between successful trials (c) plotted against the fold increase in $I_{ensemble}$ carried by 20 neurons in L2/3 (left) and L5a (right). The fold increase was obtained from each value divided by the mean value in the early sessions (sessions 1–4). Data are plotted from sessions in which ≥20 neurons were reconstructed (L2/3, n = 72 sessions from 7 fields from 6 mice; L5a n = 82 sessions from 7 fields from 6 mice). Each field is indicated by a different color. Regression lines are shown for each field. The black regression lines are for all points. Spearman's rank correlation coefficient (ρ) and P values for the regression involving all points are shown.

$I_{ensemble}$ and two task performance parameters, the success rate and the number of successful trials (success rate, one-tailed P = 0.048, Spearman's rank correlation coefficient was lower after the replacement than before that in 2,855 of 3,000 trials; successful trials, one-tailed P = 0.002, Spearman's rank correlation coefficient was lower after the replacement than before that in 2,994 of 3,000 trials; interval time, one-tailed P = 0.11, Spearman's rank correlation coefficient was lower after the replacement than before that in 2,666 of 3,000 trials). This indicates that increase neurons are critical for the correlation between L5a $I_{ensemble}$ and task performance.

To determine a subset of neurons that greatly contributed to the ensemble representation in each session, each neuron within a field in a given session was ranked according to I_{single} (ref. 20) and the rank was then normalized between 1 (top) and 100 (bottom). The I_{single} of the 20th (as normalized) ranked L2/3 neuron was not different between the early and late sessions, whereas that of the 20th ranked L5a neuron was higher in the late sessions (**Fig. 6a**). The $I_{ensemble}$ of the top 20% of ranked neurons was larger than the $I_{ensemble}$ of the bottom 50% of ranked neurons in >85% of sessions in L2/3 (69 of 79 sessions) and L5a (70 of 82 sessions). Thus, the top 20% of ranked neurons were considered to be highly ranked neurons that strongly contributed to the ensemble representation.
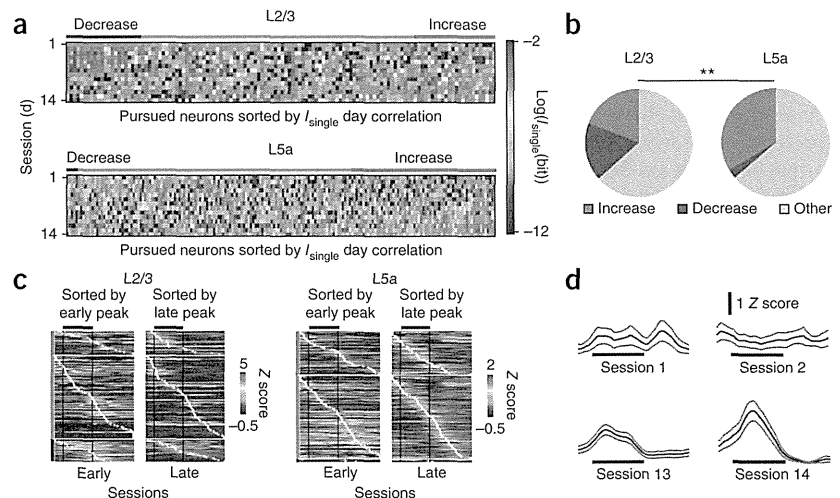
Next, we determined whether increase neurons became highly ranked neurons in the late sessions and whether highly ranked neurons in the early sessions remained highly ranked in the late sessions
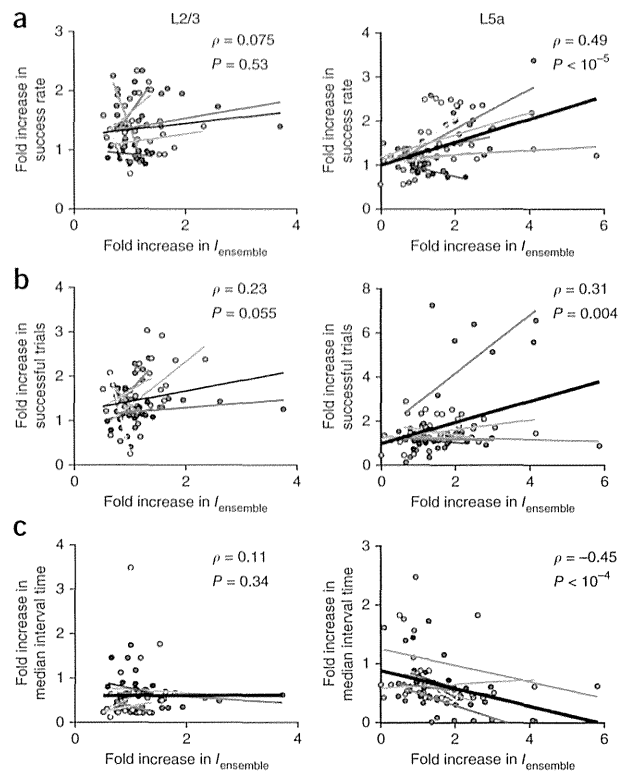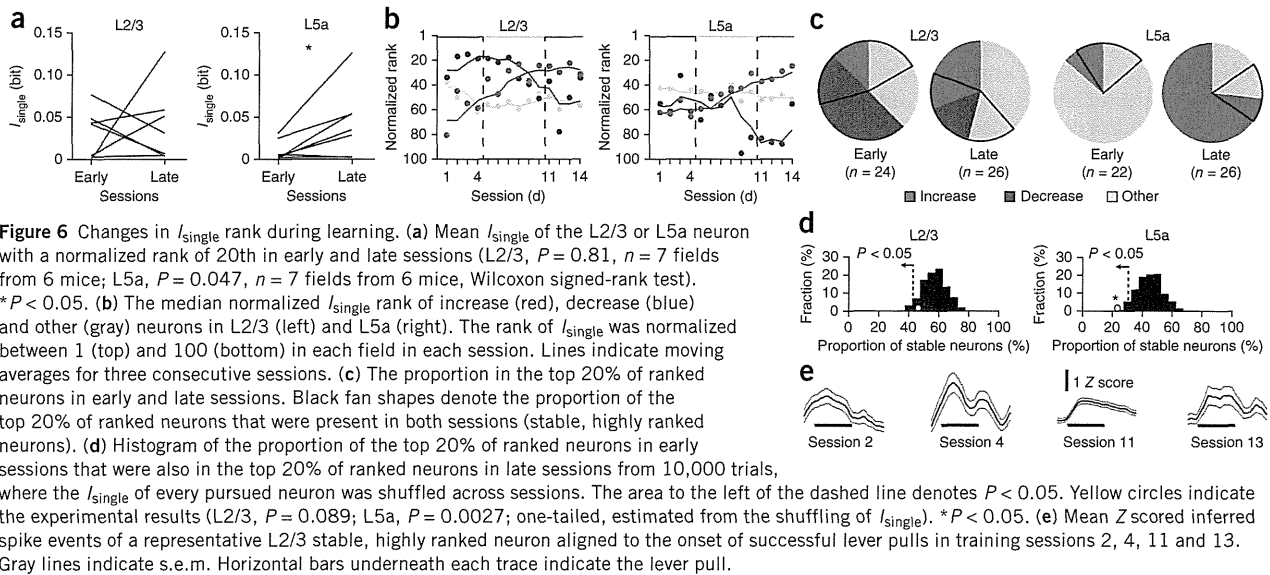
(rank stable). L2/3 increase neurons rose through the ranks from the early sessions to occupy 31% of the top 20% of ranked neurons in the late sessions (**Fig. 6b,c**). We found that 46% of the top 20% of ranked neurons in the early sessions were also in the top 20% of ranked neurons in the late sessions (**Fig. 6c**). This proportion was not smaller than the 500th lowest value of 10,000 data calculated from the shuffling of I_{single} across sessions (this is equivalent to a one-sided P value of 0.05; **Fig. 6d**). We refer to these neurons stable, highly

Figure 5 Changes in I_{single} during learning. (a) I_{single} of each pursued neuron in L2/3 (top) and L5a (bottom) in each session. The color denotes the logarithm of I_{single}. Sessions in which I_{single} could not be calculated or was approximated to zero (11 data points in L5a) are shown in gray. Blue and red bars indicate decrease and increase neurons, respectively. (b) Proportion of increase (red), decrease (blue), and other (gray) neurons across all fields in L2/3 (left) and L5a (right). The proportion of increase and decrease neurons (L2/3, 24 increase neurons, 22 decrease neurons, 80 other neurons; L5a, 63 increase neurons, 5 decrease neurons, 119 other neurons) was significantly different between layers (P < 10⁻⁵, $\chi^2[2]$ = 24.9, χ^2 test). **P < 0.01. (c) Mean Z scored inferred spike events averaged in early and late sessions for each pursued neuron in L2/3 and L5a. The pursued neurons are ordered according to the peak timing (white stars) of the averaged inferred spike events in early and

late sessions. Black horizontal bars indicate the successful lever-pull time (700 ms). Signals between imaging frames that were linearly interpolated every 10 ms were used to calculate the average[21]. Note that more increase neurons had activity peaks during the lever-pull time in late sessions than in early sessions. (d) Mean Z scored inferred spike events of a representative L5a increase neuron aligned to the onset of successful lever pulls in training sessions 1, 2, 13 and 14. Gray lines indicate s.e.m. Horizontal bars underneath each trace indicate the lever pull.

– 90 –

Figure 6 Changes in I_{single} rank during learning. (**a**) Mean I_{single} of the L2/3 or L5a neuron with a normalized rank of 20th in early and late sessions (L2/3, $P = 0.81$, $n = 7$ fields from 6 mice; L5a, $P = 0.047$, $n = 7$ fields from 6 mice, Wilcoxon signed-rank test). *$P < 0.05$. (**b**) The median normalized I_{single} rank of increase (red), decrease (blue) and other (gray) neurons in L2/3 (left) and L5a (right). The rank of I_{single} was normalized between 1 (top) and 100 (bottom) in each field in each session. Lines indicate moving averages for three consecutive sessions. (**c**) The proportion in the top 20% of ranked neurons in early and late sessions. Black fan shapes denote the proportion of the top 20% of ranked neurons that were present in both sessions (stable, highly ranked neurons). (**d**) Histogram of the proportion of the top 20% of ranked neurons in early sessions that were also in the top 20% of ranked neurons in late sessions from 10,000 trials, where the I_{single} of every pursued neuron was shuffled across sessions. The area to the left of the dashed line denotes $P < 0.05$. Yellow circles indicate the experimental results (L2/3, $P = 0.089$; L5a, $P = 0.0027$; one-tailed, estimated from the shuffling of I_{single}). *$P < 0.05$. (**e**) Mean Z scored inferred spike events of a representative L2/3 stable, highly ranked neuron aligned to the onset of successful lever pulls in training sessions 2, 4, 11 and 13. Gray lines indicate s.e.m. Horizontal bars underneath each trace indicate the lever pull.

ranked neurons. The mean activity of the stable, highly ranked neurons in L2/3 during successful lever-pull movements decreased slightly, but did not significantly change from the early to late sessions (Z scored activity, 2.0 ± 1.8 in the early sessions versus 1.3 ± 1.1 in the late sessions, $P = 0.067$, $n = 11$ neurons, Wilcoxon signed-rank test; **Fig. 6e**). These results suggest that L2/3 $I_{ensemble}$ was maintained by balanced activity of increase and decrease neurons and by the activity of stable, highly ranked neurons. In contrast with L2/3, the rank of L5a increase neurons gradually increased during the middle (sessions

5–10) to late sessions (**Fig. 6b**), and increase neurons accounted for 73% of the top 20% of ranked neurons in the late sessions (**Fig. 6c**). In L5a, only 23% of the top 20% of ranked neurons in the early sessions were in the top 20% of ranked neurons in the late sessions. This proportion was smaller than the 100th lowest value of 10,000 data calculated from the shuffling of I_{single} across sessions (**Fig. 6d**). These results indicate that the increase in L5a $I_{ensemble}$ is supported by the conversion of increase neurons into highly ranked neurons during the middle to late sessions (rank-changing evolving model).

Figure 7 *In vivo* two-photon imaging of CCS and CSp neurons in L5a during learning. (**a**) rAAV2/9-Syn-hChR2-EYFP injection into the left forelimb M1 (ref. 43) yielded dense staining of axonal fibers in the right DLS. CC, cerebral cortex. Scale bar represents 1 mm. (**b**) GCaMP3 fluorescence (left), propidium iodide staining (middle) and their overlays (right) in the left forelimb M1 from the same coronal section from a mouse in which rAAV2/9-CMV-Cre and rAAV2/9-Syn-Flex-GCaMP3 were injected into the right DLS and the left forelimb M1, respectively. Scale bar represents 200 μm. (**c**) GCaMP3 fluorescence (left), propidium iodide staining (middle) and their overlays (right) in the left forelimb M1 from the same coronal section from a mouse in which rAAV2/9-CMV-Cre and rAAV2/9-Syn-Flex-GCaMP3 were injected into the spinal cord and the left forelimb M1, respectively. Scale bar represents 200 μm. (**d**) The number of successful trials performed by three mice with GCaMP3-expressing CCS neurons (brown) and the two mice with GCaMP3-expressing CSp neurons (cyan). (**e**) *In vivo* two-photon imaging of CCS neurons transduced with rAAV2/9-Syn-GCaMP3 in the left forelimb M1 at four depths from the cortical surface. In this field, fluorescent-labeled somata

(arrowheads) were identified at depths of ≥450 μm. Scale bar represents 20 μm. (**f,g**) Motion-corrected calcium transients of five L5a CCS neurons from one field (487 μm depth) in training sessions 2 and 13 (**f**), and five L5a CSp neurons from one field (519 μm depth) in training sessions 2 and 13 (**g**). Red dots denote increase neurons. Asterisk denotes a stable, highly ranked neuron.
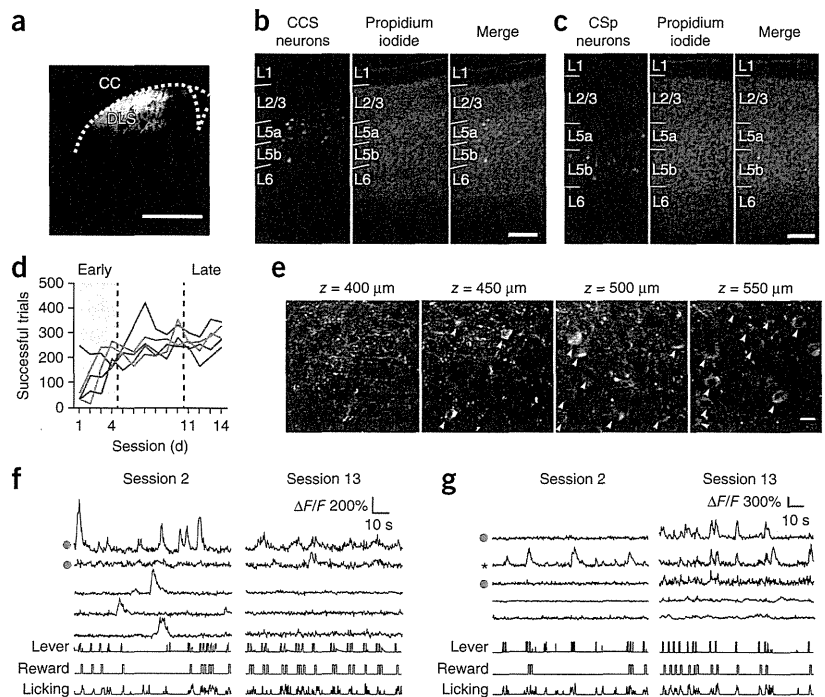
L5a and L5b of M1 project to the dorsolateral striatum (DLS; **Fig. 7a**), in which activity gradually increases during motor skill learning[33]. In L5a, crossed corticostriatal (CCS) neurons, which possess properties of intratelencephalic corticostriatal neurons, were more abundant than corticospinal (CSp) neurons[2,34] (**Fig. 7b,c**). We first determined whether the I_{single} dynamics of L5a CCS neurons during learning were the same as those of projection-unidentified L5a neurons. CCS neurons in the left forelimb M1 were retrogradely labeled[35] from the right DLS (**Fig. 7b**) and 32 CCS neurons from three mice were examined over multiple sessions (**Fig. 7d–f**). We found that 31% of the examined L5a CCS neurons (10 of 32) were increase neurons and 3% (1 of 32) were decrease neurons. Of the top 20% of the ranked CCS neurons observed in the early sessions, only 17% (1 of 6) were in the top 20% of the CCS neurons observed in the late sessions. Next, we examined I_{single} dynamics for L5a CSp neurons. CSp neurons were retrogradely labeled from the spinal cord (**Fig. 7c**) and 19 L5a CSp neurons from two mice were examined over multiple sessions (**Fig. 7d,g**). We found that 26% (5 of 19) of examined L5a CSp neurons were increase neurons and 5% (1 of 19) were decrease neurons. Of the top 20% of the ranked CSp neurons observed in the early sessions, 100% (3 of 3) were in the top 20% the CSp neurons observed in the late sessions. Although the number of the examined CCS and CSp neurons is limited, these results suggest that increase neurons are more prevalent than decrease neurons for both L5a CCS and CSp neurons. In addition, a subset of L5a CCS neurons is likely recruited into the newly formed ensemble that represents the lever-pull movement, whereas this does not occur for L5a CSp neurons.

DISCUSSION

To the best of our knowledge, these results provide the first demonstration of a distinct functional reorganization of ensemble and single-neuron activities in L2/3 and L5a during the learning of a motor task. Two-photon imaging enabled the determination of exact laminar positions, based on the cortical depth of the imaging plane and the size of the neurons, and examination of the activity of subcortical-projecting neurons. No substantial change in $I_{ensemble}$ was observed in L2/3 over the training sessions. At the single-neuron level, increase neurons were counterbalanced by decrease neurons, and a subset of neurons maintained high I_{single}. Thus, the rank-stable evolving model can be modified to a rank-stable constant model with a constant $I_{ensemble}$. In L5a, $I_{ensemble}$ improved with learning. At the single-neuron level, one-third of neurons gradually increased I_{single} during learning and strongly contributed to $I_{ensemble}$ in the late training sessions. Increase neurons accounted for 73% of the highly ranked neurons in the late sessions. This corresponds to the rank-changing evolving model.

The long-term changes in I_{single} in L2/3 and L5a could be a result of differences in cellular conditions in the early and late stages of learning. However, the number of imaged neurons, the variability in the baseline fluorescence intensity and the inferred half-decay time of the calcium transients were not different between the early and late sessions in either layer. Thus, it is unlikely that a difference in cellular conditions accounted for the changes in I_{single} in L2/3 and L5a (Online Methods).

The observation of a dynamic representation of movement by single L2/3 neurons during motor task learning is consistent with a previous report[16]. By focusing on changes in the contribution of single neurons to the ensemble coding, we found that changes in information carried by single L2/3 neurons were counterbalanced across imaged fields and that approximately 10% of neurons in L2/3 maintained high I_{single} throughout the learning process. The balanced changes in L2/3 neurons could reflect the fact that L2/3 neurons with highly plastic

activity[16] process a variety of information from other areas of the brain[6,9,10] to maintain a constant overall level of network activity for homeostasis[19,36]. At the same time, L2/3 neurons with a stable, high I_{single} may be associated with sensory feedback[21,37] that is inevitably evoked by the lever-pull movement. Alternatively, they might be associated with motor primitives[3,5] formed before the start of the learning task. L2/3 neurons may be important for rapid acquisition of novel movements or rapid adaptation to some disturbance by combining sensory feedback and motor primitives. As such, L2/3 may work as a driver for motor output throughout learning.

L5a $I_{ensemble}$ increased during learning, and this was maintained by a gradual increment in I_{single} ranks of a subset of L5a neurons (increase neurons). At the beginning of training, these L5a neurons contributed little to $I_{ensemble}$, but evolved throughout training to supersede the neurons that had a high initial contribution to $I_{ensemble}$. In the late sessions, the activity of L5a increase neurons was prominent during successful lever-pull movement, indicating that these neurons were directly associated with lever-pull movement and presumably worked as a potent driver for motor output in the late sessions. Functional reorganization in the human M1 is slow in motor learning and is presumed to represent motor memory[10]. In the motor cortex, L5 synaptogenesis and area expansion are prominent in the late stages of motor learning[11]. Activity gradually increases in the DLS during motor learning[33], whereas the dorsomedial striatum, which is innervated by the medial prefrontal cortex, is engaged at an earlier stage than the DLS[33,38]. In M1, L5a CCS neurons showed the same dynamic changes as projection-unidentified L5a neurons during learning. Thus, changes in L5a neurons in M1 may represent the formation of motor memory that accompanies memory transfer from the prefrontal area to M1 and the basal ganglia[10]. The DLS is crucial for habit formation of motor skills[33,39]. The lever-pull movement appears simple, but requires a sequence of grasping, pulling and holding by the forelimb, similar to the components of skilled forelimb food-handling behavior[21,40,41]. Thus, in the late sessions, L5a of M1 may constitute the corticostriatal system required for habit formation. In addition to CCS neurons, subcerebrally projecting neurons, including CSp neurons, also project axons to the ipsilateral striatum[34,42]. Further experiments are required to comprehensively address whether and how exactly intratelencephalically projecting neurons and subcerebrally projecting neurons constitute different learning networks with the basal ganglia[42].

L5a CSp neurons were less prevalent than L5b CSp neurons, the major motor-output neurons (**Fig. 7c**), and the number of the observed L5a CSp neurons was limited. However, if the dynamic activity changes of L5a CSp neurons represent those of CSp neurons in general, then the activity of CSp increase neurons could be increased by the L5a CCS increase neurons in the later stages of learning because CSp neurons receive synaptic inputs from L5a CCS neurons, but not vice versa[34]. Stable, highly ranked CSp neurons may be directly associated with muscle movements or motor primitives[3,5]. These neurons could be synaptically driven by the highly ranked L2/3 neurons throughout learning because CSp neurons can receive strong direct input from L2/3 neurons[2]. The distinct dynamic networks in L2/3 and L5a, the two intermediate layers of M1, would be core elements that drive the L5b motor output for well-learned movements.

METHODS

Methods and any associated references are available in the online version of the paper.

ARTICLES

AUTHOR CONTRIBUTIONS

Y.M., Y.R.T. and M.M. designed the experiments. Y.M., Y.R.T. and Y.H.T. conducted the experiments. R.H., F.O., K.K. and Y.I. developed the task device. F.O. provided the image of axonal fibers in DLS. T.O. produced AAV. Y.M. and Y.R.T. analyzed data. Y.M., Y.R.T. and M.M. wrote the paper, with comments from all authors.

1. Weiler, N., Wood, L., Yu, J., Solla, S.A. & Shepherd, G.M.G. Top-down laminar organization of the excitatory network in motor cortex. *Nat. Neurosci.* **11**, 360–366 (2008).
2. Anderson, C.T., Sheets, P.L., Kiritani, T. & Shepherd, G.M.G. Sublayer-specific microcircuits of corticospinal and corticostriatal neurons in motor cortex. *Nat. Neurosci.* **13**, 739–744 (2010).
3. Thoroughman, K.A. & Shadmehr, R. Learning of action through adaptive combination of motor primitives. *Nature* **407**, 742–747 (2000).
4. Todorov, E. & Jordan, M.I. Optimal feedback control as a theory of motor coordination. *Nat. Neurosci.* **5**, 1226–1235 (2002).
5. Sing, G.C., Joiner, W.M., Nanayakkara, T., Brayanov, J.B. & Smith, M.A. Primitives for motor adaptation reflect correlated neural tuning to position and velocity. *Neuron* **64**, 575–589 (2009).
6. Scott, S.H. The computational and neural basis of voluntary motor control and planning. *Trends Cogn. Sci.* **16**, 541–549 (2012).
7. Mitz, A.R., Godschalk, M. & Wise, S.P. Learning-dependent neuronal activity in the premotor cortex: activity during the acquisition of conditional motor associations. *J. Neurosci.* **11**, 1855–1872 (1991).
8. Nudo, R.J., Milliken, G.W., Jenkins, W.M. & Merzenich, M.M. Use-dependent alterations of movement representations in primary motor cortex of adult squirrel monkeys. *J. Neurosci.* **16**, 785–807 (1996).
9. Sanes, J.N. & Donoghue, J.P. Plasticity and primary motor cortex. *Annu. Rev. Neurosci.* **23**, 393–415 (2000).
10. Ungerleider, L.G., Doyon, J. & Karni, A. Imaging brain plasticity during motor skill learning. *Neurobiol. Learn. Mem.* **78**, 553–564 (2002).
11. Kleim, J.A. et al. Cortical synaptogenesis and motor map reorganization occur during late, but not early, phase of motor skill learning. *J. Neurosci.* **24**, 628–633 (2004).
12. Laubach, M., Wessberg, J. & Nicolelis, M.A.L. Cortical ensemble activity increasingly predicts behavior outcomes during learning of a motor task. *Nature* **405**, 567–571 (2000).
13. Carmena, J.M. et al. Learning to control a brain-machine interface for reaching and grasping by primates. *PLoS Biol.* **1**, e42 (2003).
14. Cohen, D. & Nicolelis, M.A.L. Reduction of single-neuron firing uncertainty by cortical ensembles during motor skill learning. *J. Neurosci.* **24**, 3574–3582 (2004).
15. Paz, R. & Vaadia, E. Learning-induced improvement in encoding and decoding of specific movement directions by neurons in the primary motor cortex. *PLoS Biol.* **2**, e45 (2004).
16. Huber, D. et al. Multiple dynamic representations in the motor cortex during sensorimotor learning. *Nature* **484**, 473–478 (2012).
17. Rokni, U., Richardson, A.G., Bizzi, E. & Seung, H.S. Motor learning with unstable neural representations. *Neuron* **54**, 653–666 (2007).
18. Chestek, C.A. et al. Single-neuron stability during repeated reaching in macaque premotor cortex. *J. Neurosci.* **27**, 10742–10750 (2007).
19. Lütcke, H., Margolis, D.J. & Helmchen, F. Steady or changing? Long-term monitoring of neuronal population activity. *Trends Neurosci.* **36**, 375–384 (2013).
20. Carmena, J.M., Lebedev, M.A., Henriquez, C.S. & Nicolelis, M.A.L. Stable ensemble performance with single-neuron variability during reaching movements in primates. *J. Neurosci.* **25**, 10712–10716 (2005).
21. Hira, R. et al. Spatiotemporal dynamics of functional clusters of neurons in the mouse motor cortex during a voluntary movement. *J. Neurosci.* **33**, 1377–1390 (2013).
22. Tennant, K.A. et al. The organization of the forelimb representation of the C57BL/6 mouse motor cortex as defined by intracortical microstimulation and cytoarchitecture. *Cereb. Cortex* **21**, 865–876 (2011).
23. Isomura, Y., Harukuni, R., Takekawa, T., Aizawa, H. & Fukai, T. Microcircuitry coordination of cortical motor information in self-initiation of voluntary movements. *Nat. Neurosci.* **12**, 1586–1593 (2009).
24. Tian, L. et al. Imaging neural activity in worms, flies and mice with improved GCaMP calcium indicators. *Nat. Methods* **6**, 875–881 (2009).
25. Thévenaz, P., Ruttimann, U.E. & Unser, M. A pyramid approach to subpixel registration based on intensity. *IEEE Trans. Image Process.* **7**, 27–41 (1998).
26. Dombeck, D.A., Khabbaz, A.N., Collman, F., Adelman, T.L. & Tank, D.W. Imaging large-scale neural activity with cellular resolution in awake, mobile mice. *Neuron* **56**, 43–57 (2007).
27. Vogelstein, J.T. et al. Spike inference from calcium imaging using sequential monte carlo methods. *Biophys. J.* **97**, 636–655 (2009).
28. Drucker, H., Burges, C.J.C., Kaufman, L., Smola, A. & Vapnik, V. Support vector regression machines. *Adv. Neural Inf. Process. Syst.* **9**, 155–161 (1997).
29. Nelson, R.B. An Introduction to Copulas, 2nd edn. (Springer, New York, 2006).
30. Davy, M. & Doucet, A. Copulas: a new insight into positive time-frequency distributions. *IEEE Signal Process. Lett.* **10**, 215–218 (2003).
31. Wessberg, J. et al. Real-time prediction of hand trajectory by ensembles of cortical neurons in primates. *Nature* **408**, 361–365 (2000).
32. Isomura, Y. et al. Reward-modulated motor information in identified striatum neurons. *J. Neurosci.* **33**, 10209–10220 (2013).
33. Yin, H.H. et al. Dynamic reorganization of striatal circuits during the acquisition and consolidation of a skill. *Nat. Neurosci.* **12**, 333–341 (2009).
34. Kiritani, T., Wickersham, I.R., Seung, H.S. & Shepherd, G.M. Hierarchical connectivity and connection-specific dynamics in the corticospinal-corticostriatal microcircuit in mouse motor cortex. *J. Neurosci.* **32**, 4992–5001 (2012).
35. Masamizu, Y. et al. Local and retrograde gene transfer into primate neuronal pathways via adeno-associated virus serotype 8 and 9. *Neuroscience* **193**, 249–258 (2011).
36. Abbott, L.F. & Nelson, S.B. Synaptic plasticity: taming the beast. *Nat. Neurosci.* **3**, 1178–1183 (2000).
37. Mao, T. et al. Long-range neuronal circuits underlying the interaction between sensory and motor cortex. *Neuron* **72**, 111–123 (2011).
38. Thorn, C.A., Atallah, H., Howe, M. & Graybiel, A.M. Differential dynamics of activity changes in dorsolateral and dorsomedial striatal loops during learning. *Neuron* **66**, 781–795 (2010).
39. Yin, H.H. & Knowlton, B.J. The role of the basal ganglia in habit formation. *Nat. Rev. Neurosci.* **7**, 464–476 (2006).
40. Iwaniuk, A.N. & Whishaw, I.Q. On the origin of skilled forelimb movements. *Trends Neurosci.* **23**, 372–376 (2000).
41. Kimura, R. et al. Reinforcing operandum: rapid and reliable learning of skilled forelimb movements by head-fixed rodents. *J. Neurophysiol.* **108**, 1781–1792 (2012).
42. Morishima, M. & Kawaguchi, Y. Recurrent connection patterns of corticostriatal pyramidal cells in frontal cortex. *J. Neurosci.* **26**, 4394–4405 (2006).
43. Hira, R. et al. In vivo optogenetic tracing of functional corticocortical connections between motor forelimb areas. *Front. Neural Circuits* **7**, 55 (2013).

ONLINE METHODS

Animals. The Institutional Animal Care and Use Committee of the National Institutes of Natural Sciences, Japan, approved all experiments. 2-month-old C57BL/6 male mice were used. All mice were provided with food and water *ad libitum* in a 12-h:12-h light-dark cycle and were not used for other experiments before the present study. A head plate was attached to the skull using dental cement (Fujiryu-to BC; GC, Bistite II; Tokuyama Dental) and the surface of the intact skull was subsequently coated with dental adhesive resin cement (Super bond; Sun Medical), as described previously[21]. Mice were allowed to recover for 1 d before virus injections. The number of mice per cage was 2–5 before the head plate was attached. After that, mice were single caged to avoid damaging the head plate and the glass window.

Virus production. GCaMP3 cDNA was cloned from the GCaMP3 vector and inserted into pAAV to obtain recombinant AAV2/1 (rAAV2/1) expressing GCaMP3. The vector plasmid contained GCaMP3 cDNA and the woodchuck hepatitis virus post-transcriptional regulatory element, which was expressed under control of the pan-neuronal human synapsin I promoter (Syn-GCaMP3). rAAV2/1-Syn-GCaMP3 was produced with pAAV2-1 and purified, according to previous studies[35,44,45]. All rAAV2/9 were obtained from the University of Pennsylvania Gene Therapy Program Vector Core.

Virus injection. 1 h before surgery, dexamethasone sodium phosphate (1.32 mg per kg of body weight; to prevent cerebral edema), sulfadiazine (24 mg per kg) and trimethoprim (4.8 mg per kg) antibiotics, and an anti-inflammatory, carprofen (6 mg per kg), were administered intraperitoneally[46]. Isoflurane (1%) inhalation was used for anesthesia throughout surgery. A 2-mm diameter circular craniotomy was made over the left forelimb M1 (circle centered at ~0.2 mm anterior and ~1.2 mm lateral to bregma)[21,22]. In all cases except for two L2/3 fields, the dura mater was removed[47], as the dura mater reduced L5a fluorescence. Mice were randomly chosen for imaging L2/3, L5a or both. Before virus injections, a pulled glass pipette (broken and beveled to 25–30-μm outer diameter; Sutter Instruments) and a 5-μl Hamilton syringe were back-filled with mineral oil (Nacalai Tesque) and front-loaded with virus solution. Between 0.25 and 1 μl of rAAV2/1-Syn-GCaMP3 (2.76×10^{13} vector genomes ml^{-1}) was injected at 0.1 μl min^{-1} with a syringe pump (KDS310; KD Scientific). The injection site was aimed at the left forelimb M1. To observe both L2/3 and L5a or L5a alone, the axis of the pipette was angled 30° from the horizontal plane and was advanced by 1.4 mm along the axis of the pipette[47]. To observe only L2/3, the pipette was inserted vertically approximately 300–400 μm ventral from the brain surface. After injection, the pipette was maintained in place for an additional 10 min. The pipette was then slowly withdrawn, 4% agarose L (wt/vol, Nippon Gene) was placed over the craniotomy, a 4.5-mm diameter glass coverslip (number 0 thickness; Matsunami Glass) was pressed onto the agarose surface, and the edges were sealed with the dental cement and dental adhesive resin cement. After surgery, sulfadiazine (24 mg per kg) and trimethoprim (4.8 mg per kg) antibiotics were included in drinking water, and carprofen (6 mg per kg) was administered intraperitoneally every day[46].

Labeling of CCS neurons and CSp neurons. In one mouse, 0.5 μl of rAAV2/9-Syn-GCaMP3 (9.5×10^{13} vector genomes ml^{-1}) was injected into the right DLS[2,34,35,42] (~0.1 mm posterior and ~2.5 mm lateral to bregma and ~2.5 mm ventral from the cortical surface). 4 months after the injection, a cranial window was created over the left forelimb M1. After a recovery period of 1 week, the mouse began the lever-pull task. The other two mice received an injection of 0.25 μl of rAAV2/9-CMV-Cre (6.6×10^{13} vector genomes ml^{-1}) into the right DLS (~0 mm posterior and ~2 mm lateral to bregma and ~2.5 mm ventral from the cortical surface) and, on the following day, a craniotomy was performed, 0.25 μl of rAAV2/9-Syn-Flex-GCaMP3 (1.1×10^{13} vector genomes ml^{-1}) was injected to the left forelimb M1 (700 μm ventral from the cortical surface), and a cranial window was created. After 2 weeks, the lever-pull task was initiated.

For two mice, 0.5 μl of rAAV2/9-CMV-Cre was injected to the spinal cord at the cervical level (C4, 0.3 mm right of the midline). After 5 d, 0.5 μl of rAAV2/9-Syn-Flex-GCaMP3 was injected to the left forelimb M1 (600 μm ventral from the cortical surface). Then after 4–5 weeks, the lever-pull task was initiated.

Self-initiated lever-pull task. The task was modified from a previously described procedure[21]. Mice with head plates were inserted into body chambers and their

heads were fixed in the task device for 1 h, 2 d before the start of the experiment, which allowed them to habituate to the device. After habituation, the mice were water-deprived in their home cages, and were maintained at 80–85% of their normal weight throughout the experiments. Immediately before the start of the first training session, mice were given several 4-μl drops of water from a spout near their mouths to recognize water delivery from the spout. Then, when mice pulled the lever 5 mm for 700 ms using their right forelimb, they were rewarded with a 4-μl drop of water from the spout and the lever was quickly brought back to the wait position by the force of a solenoid valve. After the lever returned it could not be moved from the wait position for 1 s. Mice were then allowed to pull the lever again. If the lever was not pulled sufficiently, a weak magnetic force (~0.03 N) returned it to the wait position; thus, mice had to maintain the lever pull for 700 ms to receive the reward. After failed trials (less than 700 ms lever pull), the lever was not immobilized and the mice were allowed to pull the lever at any time. Each mouse was trained to perform the task for 1 h d^{-1} for 14 consecutive days. The experimental time was in the light cycle. The task parameters were constant across 14 training sessions to compare cellular activity across sessions in the same task condition, in contrast with our previous study[21], in which the lever pull time was gradually increased during training sessions. A program written with LabVIEW (National Instruments) was used to regulate the timing of the reward, the lever return and lever immobilization. The lever position and the solenoid signal were continuously recorded[21]. Mouse behaviors were recorded with an infrared video camera at an acquisition rate of 30 Hz. After each training session, the mice were allowed *ad libitum* access to 1 ml of water until they were satiated, and were then returned to their home cages.

Two-photon imaging. During performance of the lever-pull task, mice were head-restrained under the microscope and two-photon images were acquired with a FV1000-MPE system (Olympus) and a mode-locked Ti:sapphire laser (Mai Tai DeepSee; Spectra Physics) tuned to a wavelength of 910–920 nm. For one mouse, an LSM 7 MP system (Carl Zeiss) and a mode-locked Ti:sapphire Chameleon Ultra II laser (Coherent) tuned to 920 nm were used. The imaging parameters are listed in **Supplementary Table 1**.

When the imaging plane reached a depth of 377 ± 12 μm ($n = 7$ fields from 6 mice) from the cortical surface, the size of the neuronal soma suddenly increased (**Fig. 2c**). L5a imaging was performed at a depth of 126 ± 27 μm ($n = 7$ fields from 6 mice) from this point. The imaged field was 382 ± 124 μm $\times$ 367 ± 148 μm (pixel size, 1.47 ± 0.53 μm $\times 2.83 \pm 1.23$ μm) at a depth below the cortical surface of 193 ± 19 μm ($n = 7$ fields from 6 mice) in L2/3, and 416 ± 111 μm $\times 426 \pm 98$ μm (pixel size, 1.62 ± 0.46 μm $\times 3.09 \pm 1.18$ μm) at a depth of 503 ± 29 μm ($n = 7$ fields from 6 mice) in L5a. Frame duration was 240 ± 42 ms ($n = 7$ fields from 6 mice) in L2/3 and 240 ± 42 ms ($n = 7$ fields from 6 mice) in L5a. Continuous 1,000 or 1,500 frame imaging was repeated one to four times in each field per session for 14 consecutive days. The total imaging duration of each field per session was 13 ± 2 min ($n = 7$ fields from 6 mice) in L2/3 and 11 ± 3 min ($n = 7$ fields from 6 mice) in L5a. If a slow z drift was detected by visual inspection, the imaging plane was manually corrected every 1,000 or 1,500 frames to fit the reference image frame that was acquired before each imaging session.

For each session, the laser intensity was adjusted to maintain a relatively constant neuronal fluorescence intensity (25–60 mW in L2/3 and 76–114 mW in L5a). The laser power for L5a imaging was relatively high compared to that used for L2/3 to L5 imaging in previous studies (10–90 mW (ref. 48) and <50 mW (ref. 49)), but, taking into account the effects of light scattering[50,51], it was comparable to a power of <70 mW for long-term L2/3 imaging[16]. The number, morphology and the coefficient of variation of baseline intensity of the imaged L5a neurons were not different between the early and late sessions. Thus, the 14-d imaging period for L5a, which used a relatively high laser intensity, likely had few detrimental effects. However, this laser intensity may have caused problems such as a slight increase in temperature that could not be detected by our measurements.

Cell-attached recording *in vivo*. 2–3 weeks after rAAV2/1-Syn-GCaMP3 injection into the L2/3 of forelimb M1, a ~3-mm diameter circular craniotomy (center: 0 mm anterior, 1.5 mm lateral to bregma) was performed under isoflurane anesthesia (1%). After the brain was covered with 2% agarose, the semi-circular glass was put on the agarose and cemented with the skull. After the mice were then recovered from anesthesia, they were given xylazine (30 mg per kg, intraperitoneal) as an analgesic and sedative. Glass microelectrodes (open-tip resistance,

5–7 MΩ) with an extracellular solution consisting of 140 mM NaCl, 4.5 mM KCl, 2 mM $CaCl_2$, 1 mM $MgCl_2$, 5 mM HEPES and 0.05 mM Alexa Fluor 594 (pH 7.4) were attached to GCaMP3-expressing neurons that were detected by simultaneous two-photon imaging[52]. The electrical signal in a loose-patch configuration (seal resistance, 25–100 MΩ) was detected with an amplifier (MultiClamp 700B; Axon Instruments), band-pass filtered at 0.5–1.5 KHz and sampled at 10 kHz. The region including the attached cell was imaged with a frame duration of 115 ± 24 ms (n = 4 regions from two mice). Calcium transient was calculated as described below, and twofold down-sampled for the subsequent analysis. Mean half-decay time of calcium transients was 491 ± 123 ms (n = 4 neurons from two mice; range: 399–664 ms). This value is consistent with previous results[24,53].

Whole-cell recording in cortical slices. Relative fluorescent changes of GCaMP3-expressing L5 neurons responding to action potentials were quantified in the slice preparation because *in vivo* cell-attached recording from the fluorescently targeted neurons in L5 is technically difficult. More than 3 weeks after the virus injection into the deep layer of forelimb M1, 500-μm-thick cortical slices containing forelimb M1 were prepared as described previously[54]. In 95% O_2/5% CO_2-saturated artificial cerebrospinal fluid containing 125 mM NaCl, 3 mM KCl, 26 mM $NaHCO_3$, 1.25 mM KH_2PO_4, 2 mM $CaCl_2$, 1 mM $MgCl_2$, and 20 mM D-glucose (pH 7.4) at 30 ± 1 °C, GCaMP3-expressing L5 neurons were recorded under whole-cell current-clamp mode with the patch-clamp electrodes (open-tip resistance, 4–8 MΩ) filled with a solution containing 135 mM potassium gluconate, 4 mM $MgCl_2$, 10 mM disodium phosphocreatine, 0.05 mM Alexa Fluor 594, 4 mM Na_2-ATP, 0.4 mM Na-GTP and 10 mM HEPES-KOH (pH 7.2, 297 mOsm). The mean resting potential of GCaMP3-expressing L5 neurons under the current-clamp recording was –65 ± 2 mV (n = 4 neurons from two mice), which was similar to that of L5 neurons from a mouse without the virus injection (–66 ± 2 mV, n = 5). The electrical signal was detected with an amplifier (AxoPatch 200A; Axon Instrument), low-pass filtered at 2 kHz and sampled at 10 kHz. The region including the recorded neuron was imaged with a frame duration of 219 ± 22 ms (n = 4).

Image processing. Analyses were performed using ImageJ (1.44k, US National Institutes of Health) and MATLAB (R2011b, 7.13.0.564, MathWorks) software. Image sequences were corrected for focal plane displacements as described previously[21,25,26]. Each motion-corrected image frame was highly correlated with the time-averaged image (time-averaged two-dimensional correlation coefficient 0.89 ± 0.06, n = 14 fields). For determining the ROI, pixels in manually defined rectangles were automatically clustered by calculating the correlation of the fluorescence intensity between pixels over time with a MATLAB-based GUI (Supplementary Fig. 1c). Attempting to construct an ROI over a neuron that did not exhibit any apparent calcium transients often resulted in pixel clusters that were inconsistent with cell morphology. Thus, the ROIs obtained by our method were restricted to active neurons. The number of reconstructed neurons per session was 52.8 ± 15.7 neurons in L2/3 and 54.1 ± 17.6 neurons in L5a. By calculating the density of neurons from Nissl staining (1,077.2 ± 59.4 mm^{-2} in L2/3, 788.4 ± 23.7 mm^{-2} in L5a; n = 5 fields for each layer from three mice), percentages of the reconstructed neurons out of all neurons in the imaged fields were estimated as 46 ± 29% of L2/3 neurons and 44 ± 11% of L5a neurons. Similar to a previous report[55], 0.6% of GCaMP3-positive neurons in L2/3 and 1.9% of GCaMP3-positive neurons in L5 were parvalbumin immunopositive (1 of 179 from four image slice planes in L2/3, n = 2 mice, and 3/162 from four image slice planes in L5, n = 2 mice), and 1.2% of GCaMP3-positive neurons in L2/3 and 0.6% of GCaMP3-positive neurons in L5 were somatostatin immunopositive (2 of 161 from four image slice planes in L2/3, n = 2 mice, and 1/175 from four image slice planes in L5, n = 2 mice). Immunohistochemistry was performed as previously described[43], with antibody to parvalbumin (mouse IgG, 1:2,000; cat. no. 235, Swant) or somatostatin (rat IgG, 1:100; cat. no. MAB354, Millipore)[56]. Thus, most reconstructed neurons were excitatory neurons.

To identify each reconstructed neuron across sessions, correlation matrices between all pairs of averaged images in different sessions were calculated, lateral displacements between each pair of the averaged images were corrected to maximize the correlation coefficients and highly correlated ROIs were shared across sessions. Although, ideally, all ROIs would be shared among all sessions, this was not possible because the imaging planes were not perfectly matched across sessions; possibly due to slight day-by-day angular displacements between the

window glass and the cortical surface. Registration of the reconstructed neurons across sessions was also visually confirmed. The difference ratio between the number of reconstructed neurons in imaging session i and the next imaging session i + 1 (N_i and N_{i+1}, respectively) was defined as ΔN_i, = $2(N_{i+1} - N_i)/(N_{i+1} + N_i)$. The mean ΔN_i was 0.026 in L2/3 (n = 72 sessions from 7 fields from 6 mice) and –0.0069 in L5a (n = 75 sessions from 7 fields from 6 mice). The mean of the absolute value of ΔN_i was 0.12 in L2/3 and 0.076 in L5a.

Averaging the fluorescence of all pixels in each ROI resulted in a raw time series, from which time-averaged background fluorescence measured at unstained blood vessels was subtracted. From this subtracted time series, the detrended relative change in fluorescence ($\Delta F/F$) was calculated with the eighth percentile value in a ± 15 s-interval around each sample time point[26]. The fluorescence time series was deconvoluted with a sequential Monte Carlo method[27] with slight modifications (dissociation constant = 542 nM and Hill coefficient = 2.73) for fitting the model to GCaMP3 kinetics[57]. When inferred by this deconvolution method, the mean half-decay time of calcium transients of the L2/3 neurons recorded in the *in vivo* cell-attached mode was 499 ± 403 ms (n = 4 neurons).

Spontaneous neuronal activity is generally higher in L5 than in L2/3 (ref. 23), and thus it may be expected that the small amount of activity associated with the lever movement would not be detected in this study. However, in a similar self-initiated lever-pull-push task of the rat, the firing rate of lever movement–related neurons increased from the baseline activity by 5–20 Hz in superficial-layer pyramidal neurons and 10–30 Hz in deep-layer pyramidal neurons during and around the time of lever movement[23]. Thus, we expected neuronal activity associated with 700-ms lever-pull movement (0.7 s × 10–30 Hz = 7–21 action potentials) to be detected as $\Delta F/F$ even in L5a in this study. A few action potentials induced only small $\Delta F/F$ (<10%) in GCaMP3; thus, the contribution of neurons that slightly changed their activity in relation to the lever-pull movement would be underestimated in this study, as previously discussed[16].

In this study, fluorescence was observed in the nucleus as well as the cytosol of the somata of many GCaMP3-expressing L5a neurons (Fig. 2e). It has been reported that L2/3 neurons with nuclear GCaMP3 fluorescence have abnormal activity[24]. However, when the expression of the protein was not too strong, L5 neurons that appeared to possess nuclear GCaMP3 fluorescence showed healthy calcium transient responses in their somata[47–49]. Our data support the latter notion. First, when CCS neurons were retrogradely labeled by rAAV2/9-Syn-GCaMP3, fluorescence was weaker than that of L5a neurons labeled by other virus injection methods and the nuclei were not filled with GCaMP3 (Fig. 7e). Their proportion of increase neurons was 2 of 6, which was the same as that in the total pursued L5a CCS neurons (10 of 32). Second, whole-cell recording from GCaMP3-expressing L5 neurons in slice preparations showed that calcium transients increased as the number of action potentials increased, such as in the *in vivo* cell-attached recordings in L2/3 (Supplementary Fig. 3c,d). In addition, the inferred decay time of calcium transients in L5a neurons was not different to that in L2/3 neurons. Thus, GCaMP3-expressing L5 neurons were physiologically healthy. Third, the inferred half-decay time in L5a neurons and the number of L5a neurons were not different in early and late sessions. The signal-to-noise ratio of $\Delta F/F$ in individual L5a neurons during non–lever-pull periods showed only a slight change from the early to late sessions (Supplementary Fig. 3f). Thus, there was no apparent degradation of GCaMP3-expressing L5a neurons over the 14 training sessions. In light of these results, we concluded that L5a neurons with nuclear fluorescence were healthy throughout the sessions, and therefore the nuclear fluorescence of L5a neurons had little, if any, effect on the experimental results.

Statistics. Data are presented as mean ± s.d. Student's t test, sign test, Wilcoxon signed-rank test, Wilcoxon rank sum test, Spearman's rank correlation test, Pearson's correlation test, χ^2 test, bootstrap tests and random permutation tests were used for statistical comparisons. For multiple comparisons in Supplementary Figure 8, Wilcoxon rank sum test with Bonferroni correction was used. No statistical methods were used to predetermine sample sizes, but our sample sizes are similar to those reported in a previous publication[16]. In statistical tests for the comparisons in the averaged half-decay time of the calcium transients and in regression lines in Supplementary Figure 6c,d, data distribution was assumed to be normal, but this was not formally tested. All statistical comparisons except for two tests were two-tailed; the results in Figure 6d and changes in the correlation between the $I_{ensemble}$ and performance parameters by

replacing increase neurons were tested with one-sided statistics. This is because the direction of the difference in these cases was predicted and the question was limited to whether the magnitude of the difference was significant or not. Data collection and analysis were not performed blind to the conditions of the experiments. However, reconstructed neurons and pursued neurons were collected as many as possible in the light of the criteria described above, which were determined before analyzing the predictive information carried by neuronal ensembles or by single neurons.

Prediction of lever movement trajectory by support vector regression and the estimation of mutual information between the recorded and predicted lever trajectories are described in **Supplementary Modeling**.

A **Supplementary Methods Checklist** is available.

44. Xiao, W. *et al.* Gene therapy vectors based on adeno-associated virus type 1. *J. Virol.* **73**, 3994–4003 (1999).
45. Okada, T. *et al.* Scalable purification of adeno-associated virus serotype 1 (AAV1) and AAV8 vectors, using dual ion-exchange adsorptive membranes. *Hum. Gene Ther.* **20**, 1013–1021 (2009).
46. Holtmaat, A. *et al.* Long-term, high-resolution imaging in the mouse neocortex through a chronic cranial window. *Nat. Protoc.* **4**, 1128–1144 (2009).
47. Mittmann, W. *et al.* Two-photon calcium imaging of evoked activity from L5 somatosensory neurons *in vivo. Nat. Neurosci.* **14**, 1089–1093 (2011).
48. Glickfeld, L.L., Andermann, M.L., Bonin, V. & Reid, R.C. Cortico-cortical projections in mouse visual cortex are functionally target specific. *Nat. Neurosci.* **16**, 219–226 (2013).
49. Keck, T. *et al.* Synaptic scaling and homeostatic plasticity in the mouse visual cortex *in vivo. Neuron* **80**, 327–334 (2013).
50. Helmchen, F. & Denk, W. Deep tissue two-photon microscopy. *Nat. Methods* **2**, 932–940 (2005).
51. Oheim, M., Beaurepaire, E., Chaigneau, E., Mertz, J. & Charpak, S. Two-photon microscopy in brain tissue: parameters influencing the imaging depth. *J. Neurosci. Methods* **111**, 29–37 (2001).
52. Kitamura, K., Judkewitz, B., Kano, M., Denk, W. & Häusser, M. Targeted patch-clamp recordings and single-cell electroporation of unlabeled neurons *in vivo. Nat. Methods* **5**, 61–67 (2008).
53. Zariwala, H.A. *et al.* A Cre-dependent GCaMP3 reporter mouse for neuronal imaging *in vivo. J. Neurosci.* **32**, 3131–3141 (2012).
54. Tanaka, Y., Tanaka, Y., Furuta, T., Yanagawa, Y. & Kaneko, T. The effects of cutting solutions on the viability of GABAergic interneurons in cerebral cortical slices of adult mice. *J. Neurosci. Methods* **171**, 118–125 (2008).
55. O'Connor, D.H., Peron, S.P., Huber, D. & Svoboda, K. Neural activity in barrel cortex underlying vibrissa-based object localization in mice. *Neuron* **67**, 1048–1061 (2010).
56. Gonchar, Y., Wang, Q. & Burkhalter, A. Multiple distinct subtypes of GABAergic neurons in mouse visual cortex identified by triple immunostaining. *Front. Neuroanat.* **1**, 3 (2007).
57. Zhao, Y. *et al.* An expanded palette of genetically encoded Ca^{2+} indicators. *Science* **333**, 1888–1891 (2011).